IV. Spacecraft Power

GUIDANCE AND CONTROL DIVISION

A. Solar Power System Definition Studies,
H. M. Wick

1. Introduction

The overall objective of the solar power system defini-
tion studies is to investigate problems associated with
the development of spacecraft power systems and to
develop the technology required to solve specific system
design problems for JPL missions. One task which is
presently being undertaken is the investigation and devel-
opment of computer programs for power system design
and analysis.

2. Shepherd's Equation Battery Discharge Computer Program

a. Method. A Fortran IV computer program has re-
cently been developed for predicting battery discharge
characteristics. Experimental data, at a constant dis-
charge current, are fitted by the program to an empirical
equation derived by C. M. Shepherd. This equation de-
scribes the battery potential during discharge as a func-
tion of discharge time, current density, and other factors.
The method used by the computer program for deter-
mining the empirical constants of Shepherd's equation is
essentially the same as described in Refs. 1 and 2.

The battery potential during discharge is given as a
function of time, current density, polarization, internal
resistance, and other factors:

$$Y = E_s - B \left(\frac{C}{C - X} \right) Z + D \exp \left(- \frac{EX}{C} \right) - LZ \tag{1}$$

Empirical values for E_s, L, B, C, D, and E are deter-
mined by the computer program by numerically fitting
experimental discharge data to the above equation. (See
Table 1 for definition of symbols.)

Battery data consisting of discharge voltage–time data,
current density, number of voltage plateaus, and plateau
base potentials are input to the program. A capacity
versus voltage curve is computed, then the empirical
constants E_s, L, B, C, D, and E for the first plateau of
the discharge curve are determined by using least-square
curve-fitting techniques. Similarly, the empirical con-
stants are computed for the second plateau, provided
that one exists. The method is flowcharted as shown in
Fig. 1.

b. Output. The first page of the output for the com-
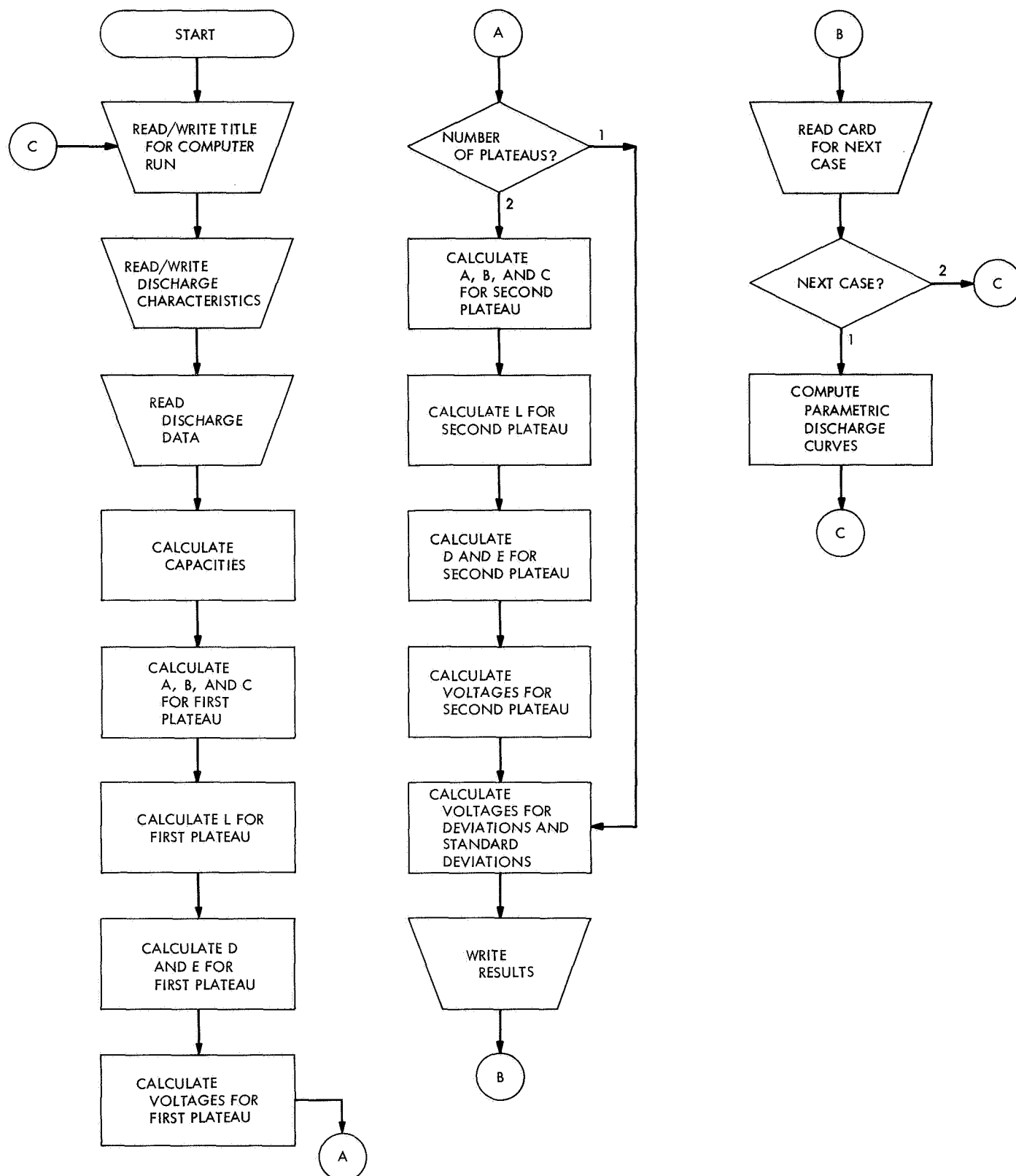puter program is shown in Fig. 2. Lines one through

Fig. 1. Flowchart of Shepherd's equation battery discharge computer program

```
DELCO-REMY SILVER-ZINC 13 PLATE CELL      TEMP. = 75 F    HMW                 N3=N2
```

Z	ES1	ES2	NP	N1	N2	N3	N4
2.0000E 00	1.8600E 00	1.6000E 00	2	5	13	13	24

A1	B1	C1	D1	E1	L1
1.8942E 00	3.6682E-02	1.4654E 01	4.3349E-02	7.7696E 00	-1.7115E-02

A2	B2	C2	D2	E2	L2
1.5705E 00	1.9135E-03	4.5443E 01	0.0000E-39	0.0000E-39	1.4735E-02

T	X	V	Y	Y-V
0.0000E-39	0.0000E-39	1.8750E 00	1.8642E 00	-1.0785E-02
5.0000E-01	1.0000E 00	1.8400E 00	1.8410E 00	1.0028E-03
1.0000E 00	2.0000E 00	1.8200E 00	1.8243E 00	4.2825E-03
1.5000E 00	3.0000E 00	1.8100E 00	1.8108E 00	8.1447E-04
2.0000E 00	4.0000E 00	1.8000E 00	1.7985E 00	-1.4799E-03
2.5000E 00	5.0000E 00	1.7850E 00	1.7859E 00	9.2790E-04
3.0000E 00	6.0000E 00	1.7700E 00	1.7718E 00	1.8004E-03
3.6000E 00	7.2000E 00	1.7500E 00	1.7510E 00	9.5287E-04
4.0000E 00	8.0000E 00	1.7300E 00	1.7333E 00	3.2824E-03
4.6000E 00	9.2000E 00	1.7000E 00	1.6974E 00	-2.5614E-03
5.0000E 00	1.0000E 01	1.6600E 00	1.6634E 00	3.4391E-03
5.3000E 00	1.0600E 01	1.6300E 00	1.6292E 00	-8.1067E-04
5.5000E 00	1.1000E 01	1.6000E 00	1.6001E 00	1.2706E-04
5.7000E 00	1.1400E 01	1.5800E 00	1.5654E 00	-1.4578E-02
6.0000E 00	1.2000E 01	1.5700E 00	1.5653E 00	-4.6692E-03
7.0000E 00	1.4000E 01	1.5650E 00	1.5650E 00	-1.4901E-08
8.0000E 00	1.6000E 01	1.5650E 00	1.5646E 00	-3.7572E-04
1.0000E 01	2.0000E 01	1.5600E 00	1.5637E 00	3.6957E-03
1.2000E 01	2.4000E 01	1.5550E 00	1.5624E 00	7.4206E-03
1.4000E 01	2.8000E 01	1.5500E 00	1.5606E 00	1.0561E-02
1.6000E 01	3.2000E 01	1.5450E 00	1.5576E 00	1.2594E-02
2.1000E 01	4.2000E 01	1.5350E 00	1.5200E 00	-1.4982E-02
2.2000E 01	4.4000E 01	1.4500E 00	1.4500E 00	-1.4901E-08
2.2400E 01	4.4800E 01	1.3000E 00	1.3000E 00	0.0000E-39

```
AVERAGE DEVIATION =      6.3611E-03
```

Fig. 2. Typical output from Shepherd's equation battery discharge computer program, showing empirical constants and accuracy of curve fit

Table 1. Nomenclature

Y	battery potential during discharge, V
A	$E_s - LZ$
B	polarization coefficient, $\Omega\text{-cm}^2$
C	available active material, C/unit area
X	energy removed from battery during time t
Z	current density, A/cm^2
E_s	constant base potential, V
L	internal resistance/unit area, Ω/cm^2
D	empirical constant
E	empirical constant
$ES1$	first plateau base potential
$ES2$	second plateau base potential

Fig. 3. Comparison of actual discharge curve and predicted curve (I = 2 A)

Fig. 4. Comparison of actual discharge curve and predicted curve (I = 5 A)

three of the printout identify the battery, current density, number of plateaus, number of data points inputted for each plateau, location of the end of the first plateau and beginning of the second plateau, and the plateau base potentials. The empirical constants required in Shepherd's equation, and computed by the program, are printed on lines four through seven. The remaining information contained in the printout consists of discharge voltage, time, capacity removed, and computed terminal voltage Y. The last column of this printout lists the difference between the measured voltage and computed voltage. This difference is useful in determining how well Shepherd's equation describes the inputted battery discharge curve.

Using Shepherd's equation computer program, a parametric discharge curve was predicted for a discharge current of 2 A. Figure 3 shows this predicted curve plotted with the actual discharge curve at 2 A obtained from experimental data. Figure 4 compares the predicted discharge curve for a discharge current density of 5 A with the actual discharge curve at 5 A. In this case, Shepherd's equation constants were evaluated from the 2 A case.

3. Conclusion

This computer program provides an excellent means for modeling a wide variety of battery or cell discharge characteristics through the use of Shepherd's equation. It provides a complete description of battery discharge characteristics, using a minimum of experimental data, and facilitates the pinpointing of experimental error in the discharge data. Capacity and discharge voltage can
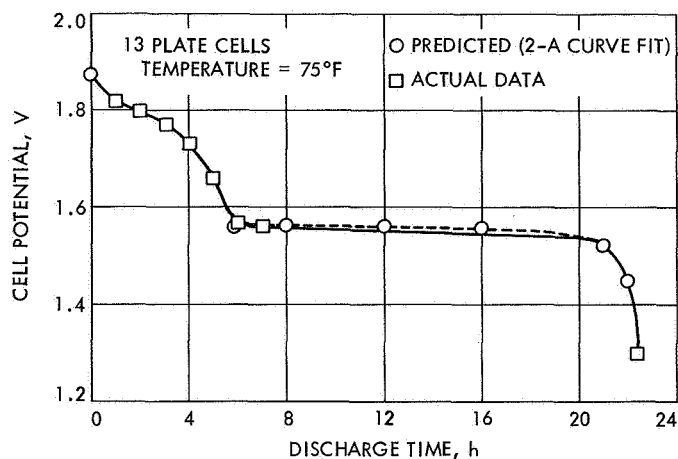
be predicted for a wide range of current densities by a single equation. This greatly facilitates battery analysis for the power systems engineer.

References

1. Shepherd, C. M., *Theoretical Design of Primary and Secondary Cells, Part III—Battery Discharge Equation*, Report 5908. U. S. Naval Research Laboratory, May 2, 1963.

2. Shepherd, C. M., "Design of Primary and Secondary Cells, II. An Equation Describing Battery Discharge," *J. Electrochem. Soc.*, Vol. 112, No. 7, July 1965.

B. Mars Spacecraft Power System Development, H. M. Wick

1. Introduction

A two-phase study was initiated to design an improved *Mariner* spacecraft power system for possible future Mars
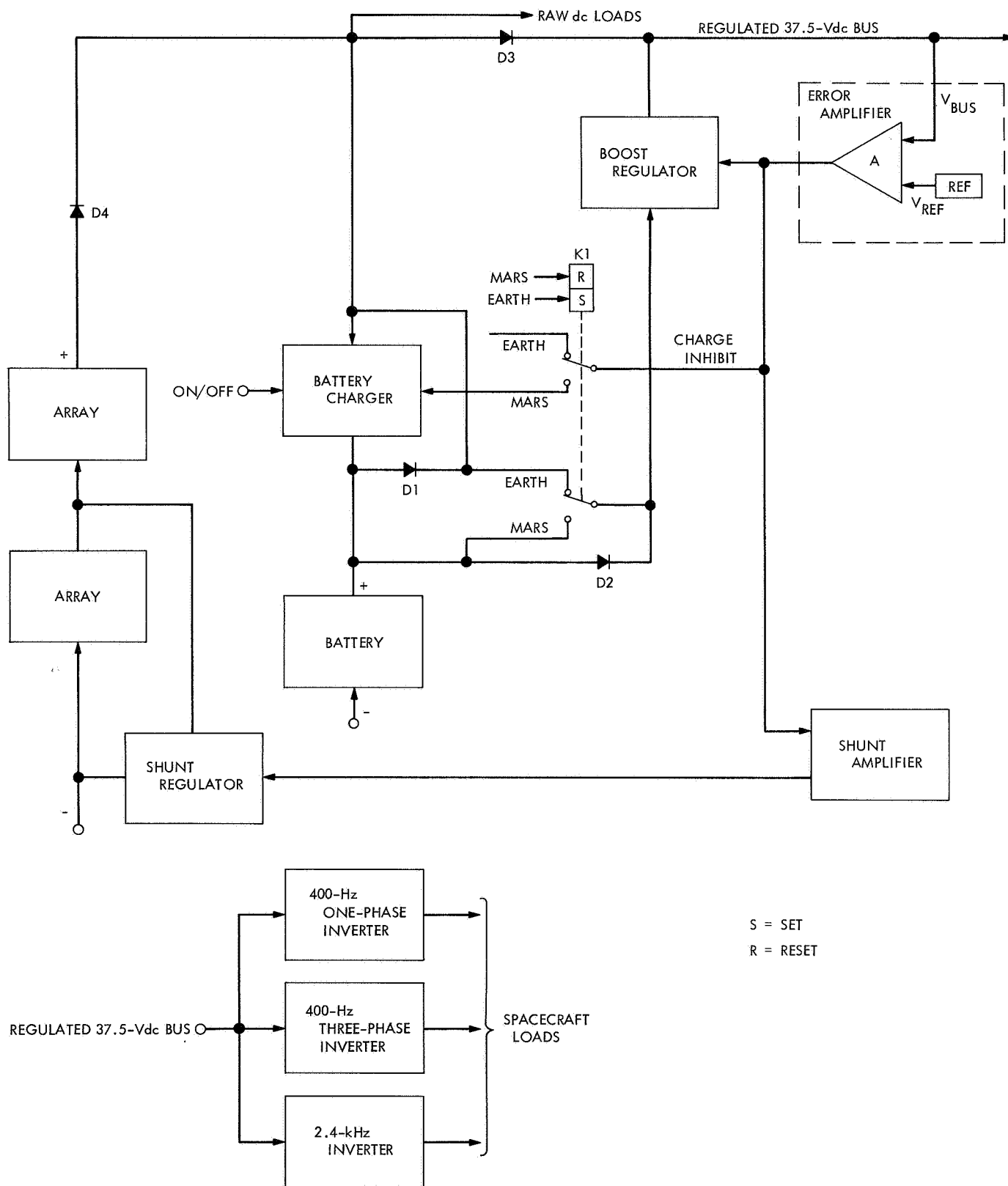
RAW dc LOADS

REGULATED 37.5-Vdc BUS

D3

ERROR AMPLIFIER

V_{BUS}

BOOST REGULATOR

A

REF

V_{REF}

K1
MARS → R
EARTH → S

ARRAY

+

D4

ON/OFF ○→

BATTERY CHARGER

EARTH

MARS

CHARGE INHIBIT

ARRAY

D1

EARTH

MARS

D2

SHUNT REGULATOR

BATTERY

+

−

−

SHUNT AMPLIFIER

400-Hz ONE-PHASE INVERTER

REGULATED 37.5-Vdc BUS ○

400-Hz THREE-PHASE INVERTER

SPACECRAFT LOADS

2.4-kHz INVERTER

S = SET
R = RESET

Fig. 5. GE shunt power system

missions. The latest system design techniques and component technology are being employed to develop optimum power systems for both Mars flyby and orbiter spacecraft.

In Phase I, General Electric Co. and TRW Systems investigated and analyzed various candidate power system designs. Each contractor then selected one power system for recommendation to JPL.

2. General Electric Co. Study

Using load power requirements supplied by JPL for a typical early 1970 Mars orbiting mission, the General Electric study resulted in the design of a shunt power system.

A functional block diagram of the shunt regulation system is shown in Fig. 5. Inverter power (both 2.4 kHz and 400 Hz) is derived from a regulated 37.5-V dc bus. Direct-current regulation of this bus is maintained by sequentially controlling the array shunt regulators, battery charger, and the boost regulator in response to separate regions (Fig. 6) of an error amplifier input voltage (see upper right of Fig. 5). The shunt regulator operates in the highest error region with maximum solar array shunting occurring at V_4 down to little or no shunting at V_3. At this voltage, the available array power at the

Fig. 6. Response regions of shunt, boost, and charge regulators

regulated bus just satisfies the spacecraft load demand along with any battery charging power that may be required. Increased load demands or a decrease in available solar array power cause the battery charging power to be diverted to the load to maintain regulation. This occurs in the voltage range V_3 to V_2. With further load demands or further decrease in array power, the boost regulator comes on to maintain the regulated bus voltage between V_2 and V_1.

To reduce solar array matching problems which arise from a change in the array current–voltage characteristics in the earth-to-Mars transit, diode D3 and relay K1 (Fig. 5) have been incorporated in the design of the shunt system. The solar array power–voltage characteristics shown in Fig. 7 help to illustrate the nature of this problem. For the 1.5-AU curve (Fig. 7), which is typical for a Mars orbiting mission 90 days after encounter, the normalized voltage at the maximum power point is 1.3 V. If the system-regulated voltage is selected to be 1.3 V or higher, no power would be available at this voltage from the solar array near earth (1.0 AU). By selecting a system voltage of 1.2 V, equivalent power can be obtained for the 1.5- and 1.0-AU conditions but with a sacrifice in the power at 1.5 AU of about 6%. The in-line diode D3 and the earth/Mars mode relay K1 solve this problem.

During launch and the early cruise phase, K1 is set in the "earth" position. If the solar array voltage is low, the boost regulator operates to maintain voltage regulation. When array voltage is high, the regulated dc bus voltage is maintained by the shunt regulator and the array current passes directly through diode D3. In both cases, battery discharge diodes D1 and D2 are back-biased.

Approximately 2 mo after launch, the change in array characteristics permits transferring the earth/Mars mode relay K1 to the "Mars" position M. This prevents array/battery load sharing during later phases when the solar array power capability becomes limited. Two system modes of operation will predominate.

(1) *Near earth*, the boost regulator will be operating from solar array power. Battery charging is not inhibited since array power is much greater than required to support the spacecraft power demand. The shunt regulator is "standing by" on line. During emergence from a solar occultation near earth, the shunt regulator will be operating with the boost regulator off.

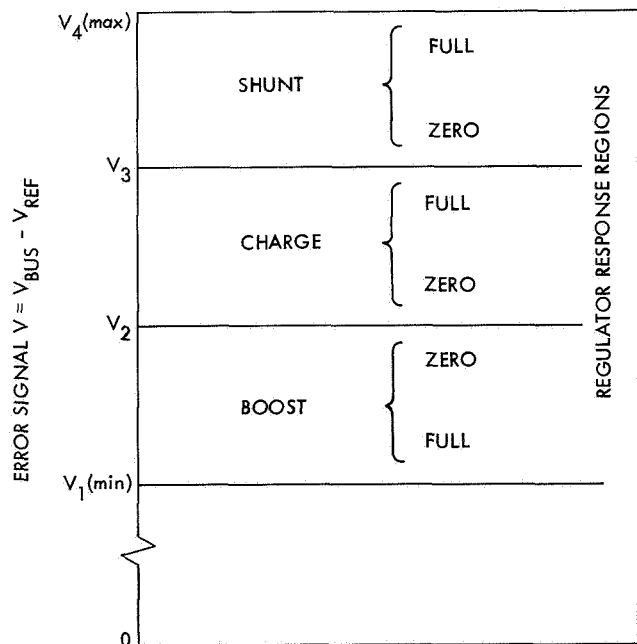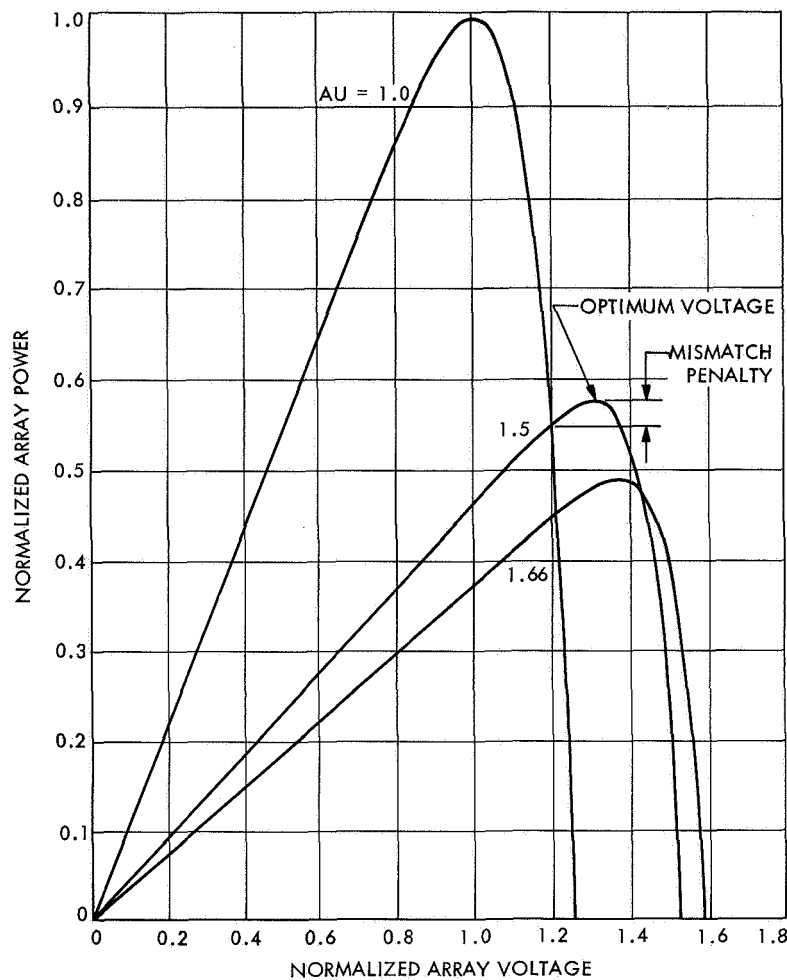(2) *Near Mars*, the shunt regulator will be operating from solar array power with the boost regulator off.

Fig. 7. Predicted *Mariner* Mars solar array
power–voltage curves

Battery charging may be inhibited, if necessary, to maintain the system-regulated voltage.

The power system design recommended by General Electric eliminates the need for the array zener diodes, share mode detector, and share boost converter; but requires the addition of the earth/Mars mode relay and the array-mounted shunt regulators. Unregulated bus voltage range has been reduced from 25–50 V dc (*Mariner* Mars 1969) to 25–38.2 V dc. The power system recommended by General Electric weighs 0.3 lb more than the present *Mariner* Mars 1969 power system.

3. TRW Systems Study

TRW recommended a buck–boost power system. A simplified block diagram of this system is shown in Fig. 8. A regulated 50-V dc bus supplies power to the 400-Hz

and 2.4-kHz inverters and to the various spacecraft dc loads (traveling-wave tube, heaters, etc.). Regulation is provided by a buck–boost line regulator. Redundant silver–zinc 25 A-h batteries have been included in the system design. Battery charging power is obtained from the regulated dc bus. A current-limiting resistor and a relay are used to control charging. Ground command backup capability is provided to override the automatic charge control circuitry that controls the relay.

Power system reliability has been enhanced through incorporation of current limiting and operational redundancy in the buck–boost regulator. The need for zener diode voltage limiters on the solar array has been eliminated. Packaging requirements reduce the number of power conditioning modules from 10 (*Mariner* Mars 1969) to 6. Power system weight has been reduced by about 4 lb.
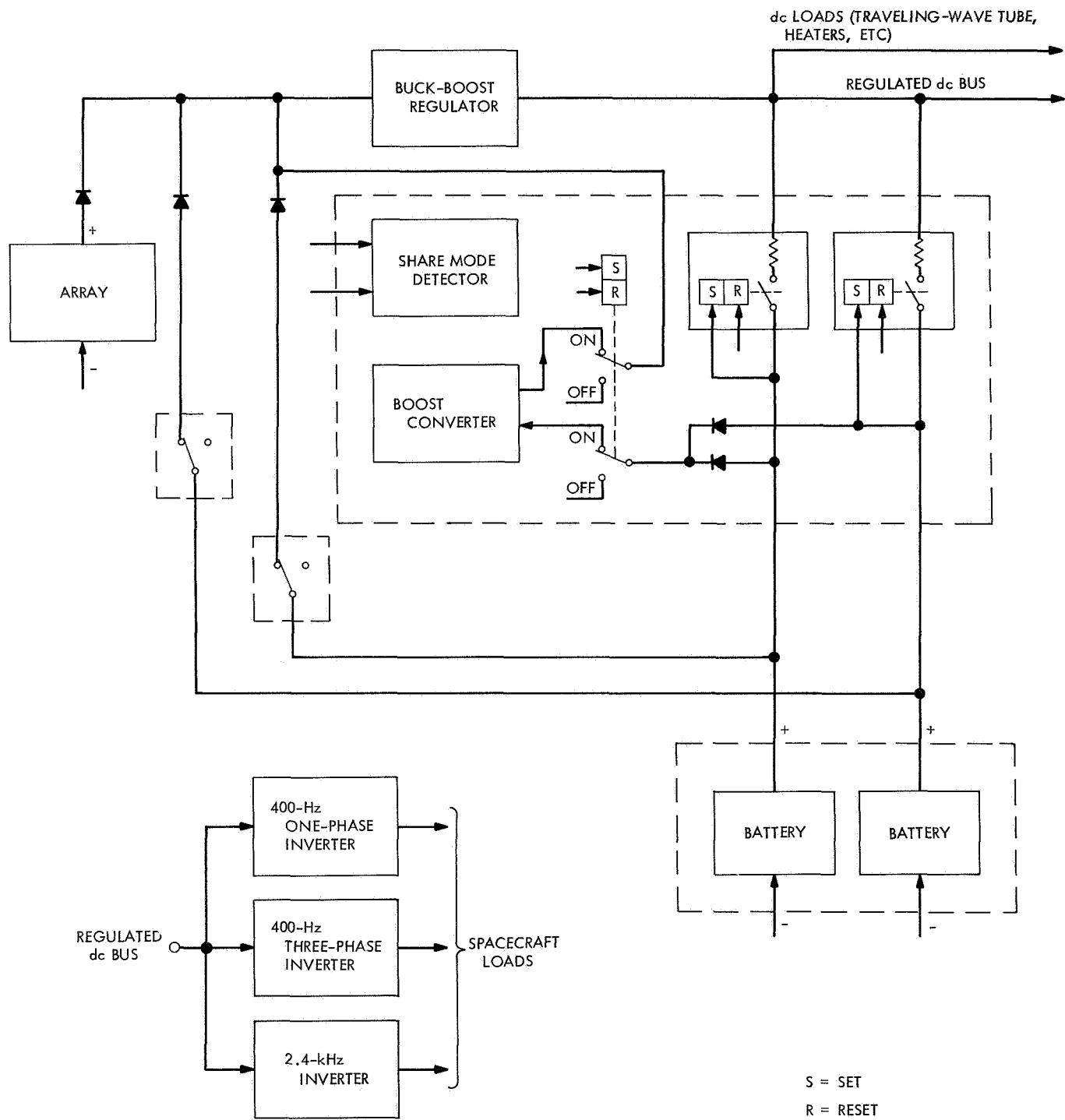
Fig. 8. TRW buck-boost power system

C. Solar Cell Contact Studies, P. A. Berman and
G. P. Rolik

1. Introduction

The purpose of these studies is to determine the characteristics of solar cell contacts, especially as a function of exposure to various environmental conditions. Many problems exist with present-day state-of-the-art titanium–silver contacts, with and without solder coating. The manufacturers have not analyzed solar cell contacts sufficiently to determine what characteristics the cells will have as a result of exposure to environmental extremes.

2. Testing

a. *Ferranti Electric, Inc. cells.* These cells have contacts fabricated by plating nickel onto the silicon and layers of copper and gold over the nickel. Forty-eight cells, 24 fabricated from 1 Ω-cm material and 24 from 10 Ω-cm, have been exposed to an environment consisting of 95% relative humidity at a temperature of 60°C for a period of 48 h.

Before and after environmental exposure, the cells were electrically tested at a cell temperature of 28 ± 1°C in a tungsten simulator having a color temperature of 2800°K and an equivalent solar intensity of approximately 100 mW/cm². The tungsten simulator will be used extensively during these studies because of the excellent stability and reproducibility of the spectral and intensity characteristics of this source. Since the nature of the measurements to be made is, for the most part, comparative (i.e., pre- and post-environmental exposure), the fact that the tungsten spectrum differs from the sunlight spectrum should not affect the analysis.

It was determined that the environmental exposure did not adversely affect the electrical characteristics of the cells. Table 2 lists the average parameter values before and after exposure for both groups of cells.

b. *Ion Physics cells.* In these cells, developed by Ion Physics under the improved solar cell contact development program, the aluminum contacts were deposited by high-vacuum sputtering. The first lot was subjected to a temperature–humidity environment of 95% relative humidity at a temperature of 80°C for 30 days.

Electrical tests before and after exposure of the cells to this rather severe environment were performed under tungsten illumination, the intensity being adjusted to

Table 2. Ni-Cu-Au contact cell characteristics before and after 48-h exposure to 95% relative humidity at 60°C

Test group/ time	Open-circuit voltage, V	Short-circuit current, mA	Current at max power, mA	Voltage at max power, V	Max power, mW	Curve power factor,[a] %
1 Ω-cm						
Before exposure	0.583	99.6	88.9	0.480	43.0	0.73
After exposure	0.584	98.7	88.7	0.477	42.4	0.73
10 Ω-cm						
Before exposure	0.542	100.3	93.0	0.436	40.6	0.74
After exposure	0.545	99.01	91.8	0.439	40.4	0.74

[a]The curve power factor is a measure of the "squareness" of the curve:

$$\text{curve power factor} = \frac{\text{max power}}{\text{short-circuit current} \times \text{open-circuit voltage}}$$

correspond to a solar intensity of 100 mW/cm². Five control cells were held back from the total lot of 15 cells. The test temperature was 28 ± 1°C. Table 3 lists the average parameter values before and after exposure for the 10 cells tested. The test results show an extremely small degradation in cell characteristics.

Visual inspection after the environmental test showed the aluminum contacts to be oxidized. It is thought that this film of Al_2O_3 is the cause of the slightly higher series resistance experienced in the post-humidity test.

A tape test utilizing Scotch 810 tape was also conducted after exposure to the humidity environment. The

Table 3. High vacuum sputtered Al contact cell characteristics before and after 30-day exposure to 95% relative humidity at 80°C

Test time	Cell series resistance, Ω	Short-circuit current, mA	Open-circuit voltage, V	Current at max power, mA	Voltage at max power, V	Max power, mW	Curve power factor, %
Before exposure	0.54	95.7	0.541	87.7	0.430	37.7	0.728
After exposure	0.63	96.7	0.541	87.8	0.429	37.7	0.714

"N" contact strip (not grids) and back sides were tested by the peel method, with the peel starting at the edges of the cells. Results showed excellent contact adherence. There was no evidence of contact material residue on the tape.

3. Conclusions

The nickel–copper–gold contact cells procured from Ferranti Electric, Inc. appear to successfully survive a 48-h exposure to a 95% relative humidity, 60°C environment. The series resistance before and after exposure was not measured, but the fact that the pre- and post-exposure curve power factors were identical strongly indicates that there was no large change in series resistance.

The high-vacuum sputtered aluminum contact cells developed by Ion Physics under JPL contract exhibited no significant electrical degradation as a result of a 30-day exposure to the severe environment of 95% relative humidity at 80°C. A slight increase in series resistance was observed, but this is believed to be primarily due to a layer of aluminum oxide which formed as a result of the test, and which acted as a thin insulating layer between the test probes and the aluminum. In many cases, it was found that a slight scraping of the contact significantly lowered the series resistance. It is anticipated that in actual flight-use the cells would be interconnected prior to such exposures so that oxidation, at least of the magnitude observed here, would not result in an increase of series resistance.

D. Solar Cell Standardization, R. F. Greenwood

1. Introduction

Standard solar cells calibrated above 97% of the earth's atmosphere using high-altitude balloons have been effectively used over the past several years to aid in the prediction of solar array output. The standard cells are mounted in modular form, permitting temperature control and providing a means to electrically load the cell and monitor its output. Two 1- × 2-cm cells or one 2- × 2-cm cell can be mounted on the module. The modular form also provides protection for the cell during normal handling and during payload impact upon balloon flight termination.

Standard solar cells are also used to aid in establishing the light intensity and evaluating the spectral content of solar simulators. Balloon-calibrated standard solar cells in conjunction with a simulator are presently being used to classify solar cells according to power output during cell procurements, thus eliminating the use of a pyrheliometer.

Cooperative efforts between JPL and other NASA and government agencies have provided standard solar cells at minimum expense for space flight programs and advanced solar cell development.

2. Description of Calibrated Solar Cells

Solar cells submitted for calibration on the 1968 balloon flight series were from several sources. The NASA Goddard Space Flight Center supplied eight modules containing 1- × 2-cm N/P Heliotek solar cells which are intended for use with the *Orbiting Astronomical Observatory* program. The German Research Satellite Corp., in cooperation with NASA Goddard Space Flight Center, submitted seven 1-cell modules, six of which were balloon-calibrated and all of which were correlated in the JPL X-25L solar simulator. Four of the cells were manufactured by Siemens AG and three by AEG-Telefunken. Both suppliers are located in West Germany.

The Air Force Aero Propulsion Laboratory supplied eight modules containing advanced development solar cells. Three modules contained ion-implanted silicon cells. Three were assembled with cadmium sulfide solar cells having an H-film (Kapton) covering, and two modules contained cadmium telluride solar cells.

Two modules fabricated by the NASA Langley Research Center to aid in solar cell calibration were included on the flights. Heliotek 1- × 2-cm N/P cells having a base resistivity of 10 Ω-cm were used in the module assembly.

The Applied Physics Laboratory submitted a solar cell and bandpass filter experiment. The experiment consisted of five solar cells and four interference-type bandpass optical filters designed to divide the solar cell response into four equal energy bands. The fifth cell was unfiltered. Calibration data from the cell-filter combinations are intended for use with laboratory solar simulators.

The Jet Propulsion Laboratory included several experimental modules, as well as modules for use on a possible *Mariner* Mars 1971 flight. A unique experiment employing a filter wheel in conjunction with four solar cells and two radiometers was flown. The radiometers, more accurately described as enclosed standard cavity active radiometers, were designed and built at JPL.

3. Results of the 1968 Balloon Flights

A series of three 80,000-ft balloon flights was conducted in the vicinity of Minneapolis, Minnesota during the months of July and August, 1968. The solar trackers which had been modified to increase the payload capacity functioned perfectly throughout the flights. Figure 9 shows the modified tracker with payload mounted for flight 1. The tracker provides space for as many as 26 solar cell modules in the event that all modules should contain a single 2- × 2-cm cell. Two additional spaces are available to accommodate temperature-monitoring modules.

Good data were returned from each flight. Also, excellent correlation with solar simulator measurements was obtained prior to and following the flights. All cells were recovered, although two modules suffered minor damage upon impact of the second flight payload. The solar tracker was extensively damaged and a spare tracker was used for the third flight.

Flight data on all solar cells have been reduced through a computer program and all modules, along with calibration data, have been returned to the respective agencies. A formal report on the 1968 balloon flights is now in progress.
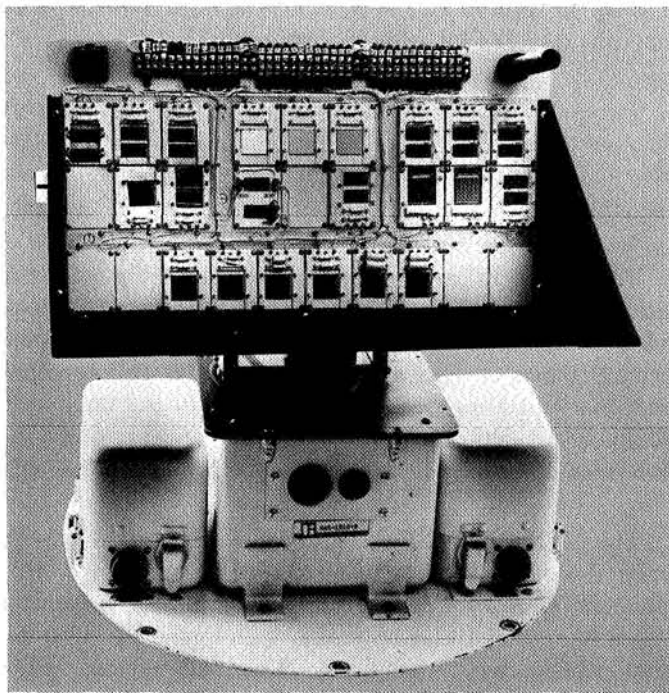

Fig. 9. Modified solar tracker

E. Advanced Roll-Up Solar Array Concept,
W. A. Hasbach

1. Program Objective

A program was initiated by JPL in June 1967 to investigate the feasibility of developing a 10-kW solar array system which would have a specific power capability of 30 W/lb and could be deployed after launch through a roll-out technique similar to that employed in a window shade.

The ever-increasing power requirements of the spacecraft, coupled with limited launch vehicle storage capacities, dictated the need to evaluate new deployment and structural designs of solar power panels. Improvement in the solar cell conversion efficiency is not anticipated in the immediate future. However, improvements in the power-to-weight ratio appear feasible using lightweight structural concepts and packaging techniques. Hence, emphasis is placed upon the mechanical–structural aspects of the solar array.

Studies performed by General Electric Co., Fairchild-Hiller Corp., and Ryan Aeronautical Co. indicate that the program objective of a 30-W/lb power-to-weight ratio system can be achieved. The total array will consist of four roll-out panels, each containing 250 ft² of deployed surface area. The four roll-out panels will be mounted symmetrically about the base of the spacecraft and will deploy uniformly without disturbing the center of gravity of the vehicle.

Previous accomplishments in this program were reported in SPS 37-48, Vol. III, pp. 51–57 and SPS 37–49, Vol. III, pp. 93–99.

2. Configuration Studies

For analysis, the roll-out array can be divided into three major components:

(1) The deployment mechanism or extendible boom.

(2) The storage drum upon which the solar cell substrate is wrapped during storage and launch.

(3) The substrate upon which the solar cells are attached.

Although the feasibility of 30 W/lb solar cell power systems appears to be within the current state-of-the-art, significant questions still exist:

(1) Will the substrate track uniformly during the retracting cycle?

(2) Will thermal cycling degrade the array output?

(3) Will the solar cell/coverglass combination be adequately protected during launch?

In this article, the greatest emphasis will be placed on the deployment mechanisms proposed by each of the three contractors. Both the substrates and storage drums are sufficiently common to all designs to allow for a general discussion of each.

During the study of deployment methods, it was noted by the three contractors that no one extendible boom system (Fig. 10) was clearly the preferred choice to achieve the desired objectives of this program. Designs selected differ broadly in concept yet still achieve the
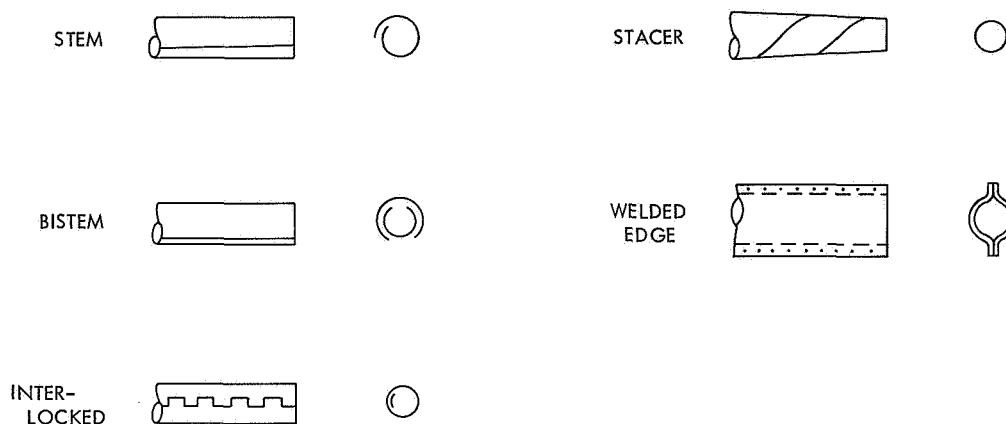
Fig. 10. Types of deployment booms
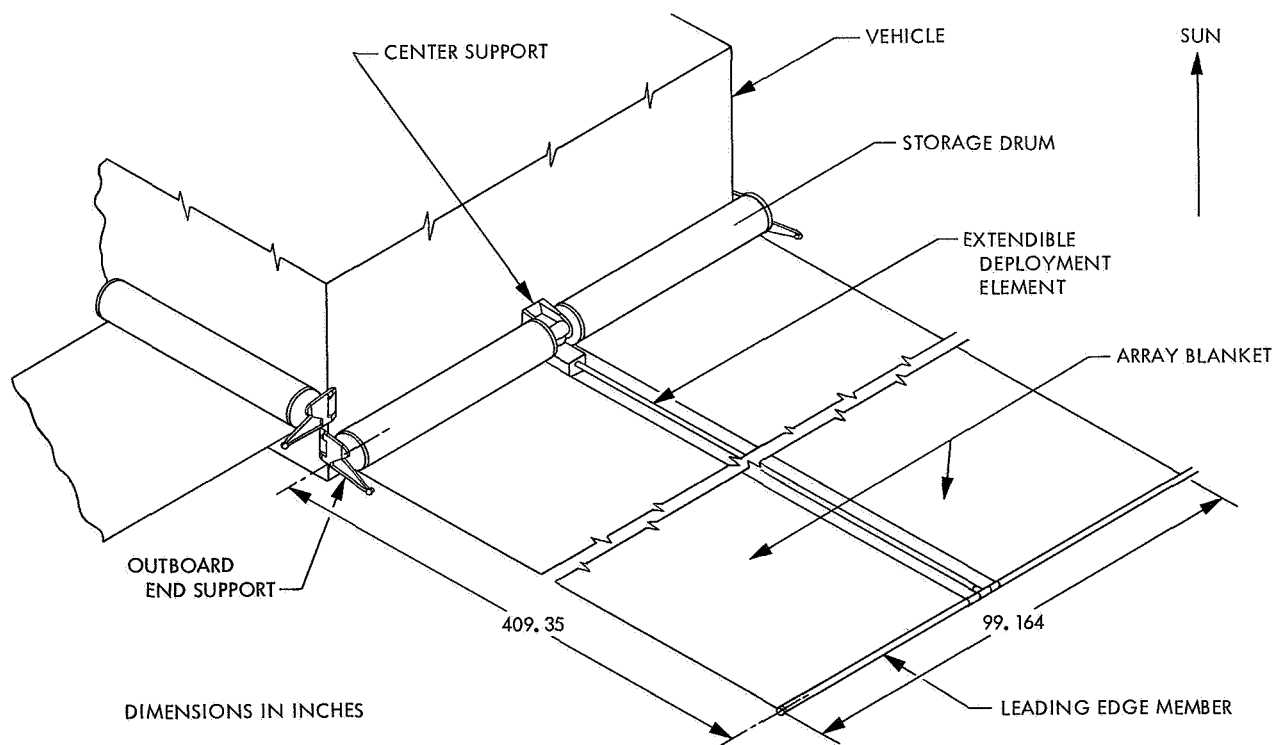
Fig. 11. Deployable 30-W/lb solar array (General Electric Co.)

30-W/lb weight requirement. Also, analysis of the various approaches has shown that they will survive the environments defined by applicable specifications.

3. Deployment Methods

a. General Electric Co. Figure 11 shows a single-rod deployment scheme, using a de Havilland bi-stem extendible element. This element consists of two stainless steel tapes which are pre-stressed and wrapped on a storage drum. As the two tapes are unrolled from the storage drum, they form tubes, one within the other. Fastened at the leading edge of the bi-stem is a cross member to which the substrate material is attached. This cross member is free to rotate through a ball bearing joint. The free floating end member is so designed as to allow the extendible rod torsional freedom during deployment. As the bi-stem rod is extended, it unrolls

the solar cell substrate from the storage drum. Positive tension is maintained on the substrate at all times by means of a "negator" spring in the storage drum. Substrate tension is required to keep the solar cell surface plane flat within 10 deg and to provide a minimum natural frequency of 0.04 Hz. To achieve these conditions, it has been calculated that a substrate tension of 4.0 lb is required.

The bi-stem is fabricated of 0.007-in.-thick No. 301 stainless steel (silver-plated). Its extended length is 33.5 ft and its diameter is 1.34 in. The extension and retraction rates are 1.5 in./s.

b. Fairchild–Hiller Corp. Figure 12 also shows a single-boom deployment system, but the extension mechanism design is considerably different from other designs investigated during this study. Deployment is accomplished
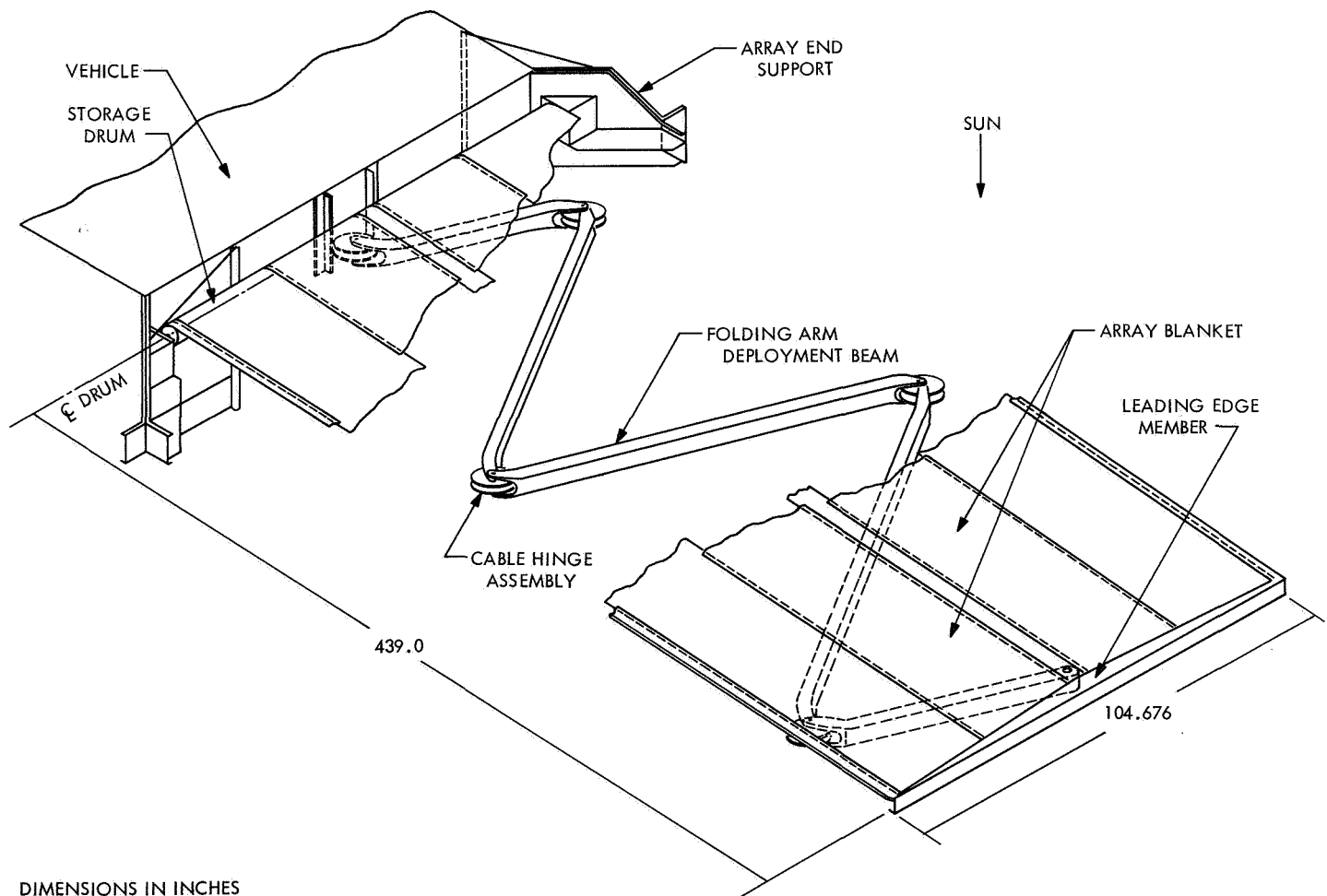

Fig. 12. Deployable 30-W/lb solar array (Fairchild–Hiller Corp.)

by means of programmed folding arms which, during the launch and stowed period, are stacked parallel to each other adjacent to the substrate storage drum. The folding arms consist of three full-length arms and two half-length arms. The half-length arms are end members of the folding arm linkage with the full arms in between. The outboard half link is pinned to the cross member which pulls the solar cell substrate from the storage drum.

Interconnecting each arm section is a fitting operated by a pulley cable arrangement. This technique is best described by comparing it to a drafting machine. In the programming of the joint action, it is essential that the arm linkages extend the end member in a straight line to avoid distorting the solar cell substrate during deployment and retraction. During deployment, tension is maintained on the substrate by means of a negator spring, as in the General Electric design, to assure a minimum natural frequency of 0.04 Hz in the substrate and to keep the substrate surface plane flat within 10 deg. To achieve these conditions, Fairchild–Hiller has determined that a force of 10.0 lb should be applied.

In the folding arm design, stainless steel, titanium, aluminum, and beryllium are used for the control cables, pulleys, and associated hardware. Boron/epoxy composites have been selected for the cross member to which

the solar cell substrate is attached and for the arm segments. The arm segments are corrugated 3.0-in.² tubes with a wall thickness of 0.911 in. When extended, the total length of the arms is 39.1 ft. The deployment and retraction rates are not yet established.

c. *Ryan Aeronautical Co.* Figure 13 shows a system using two deployment booms. Unlike the General Electric and Fairchild–Hiller systems, the solar cell substrate is fastened between the two booms, along the edges, by means of tabs at intervals of approximately 4.0 in. The two booms, which collapse as they are wound about a drum, store on the same drum as the solar cell substrate.

The booms are pre-stressed titanium, constructed of identical halves, welded along their entire length. In their natural state, the two halves are expanded, forming a hollow tube. When compressed, they can be wrapped tightly about a drum or cylinder.

As the booms are deployed, the solar cell substrate is carried off of the same storage drum. No substrate tension is considered necessary because of the edge support by the two-beam system. Thermal deflection is maintained within the allowed 10-deg bending, by sizing of the two beams and thermal control coating.
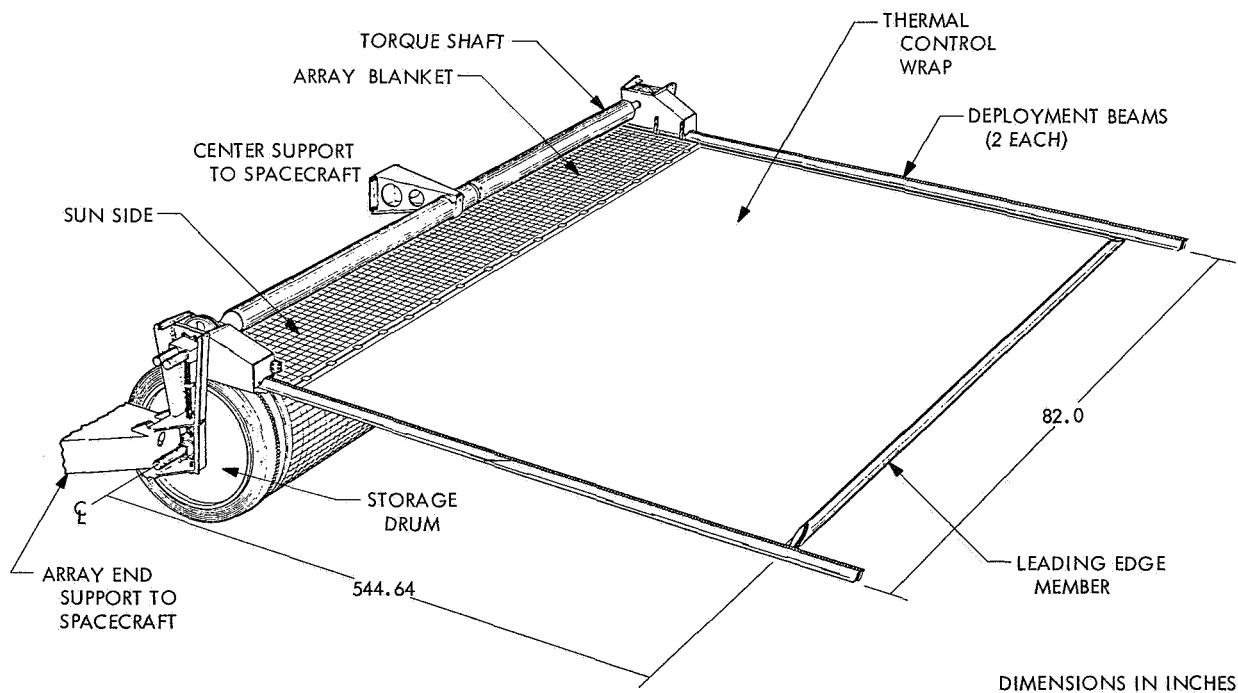

Fig. 13. Deployable 30-W/lb solar array (Ryan Aeronautical Co.)

The two booms, constructed of 0.003-in.-thick titanium, form an oval pattern 2.2 × 1.7 in. in the expanded condition. In the fully deployed condition, the booms are extended to 33 ft. The deployment and retraction rate is 1.7 in./s.

4. Substrate Materials

During the materials selection effort of this program, the contractors evaluated various candidate substrate materials; the two most promising were fiberglass and Dupont Kapton H-film. Kapton H-film was selected for its greater tear resistance, greater flexible strength, and strength-to-weight advantage.

Because of the two-boom system selected, Ryan can manufacture the substrates of 0.001-in.-thick H-film. General Electric, with a substrate tension of 4.0 lb, has selected 0.002-in. H-film. Fairchild–Hiller, having the highest substrate tension of 10 lb, is using 0.003-in. H-film.

5. Storage Drum

Each contractor will use a cylindrical drum upon which the solar cell substrate will be stored. The drums vary in diameter from 5.0 to 12.0 in.

Choice of drum material by the contractor is optional inasmuch as the materials chosen can be used interchangeably between the three designs without a significant weight penalty. With the exception of the graphite/epoxy composite material used by Fairchild–Hiller, all materials are available and considered state-of-the-art. Composite materials have limited acceptance in proven applications. General Electric has specified beryllium; Ryan has specified either beryllium or titanium as drum materials.

F. Planetary Solar Array Development,
W. A. Hasbach

Trade-off studies of weight, power capabilities, and structural integrity versus exposure to the Martian environment have resulted in the selection of a preferred solar array design for a soft lander capsule. Although studies have confirmed three possible approaches which have the potential of meeting the program objective, one is felt to be more worthy of further investigation. The non-oriented conical truncated cone (Fig. 14) was selected as the most feasible design because of its higher

reliability factor, best compromise in power versus weight, absence of electrical motor gear drives, no power requirement necessary for operation, and its design growth potential; this array, once released from its locked, launched, and flight position, will require no power from the lander capsule for deployment or continuous operation for the mission life of 1 yr. A summary of earlier studies of the three possible approaches appears in SPS 37-51, Vol. III, pp. 37–41.

The non-oriented conical truncated cone array, as recognized initially in its concept, will not meet the desired goal of 20 W/lb (1 AU) and under worst-case conditions will attain less than the minimum power requirement of 200 W of electrical power at solar noon. On the other hand, Figs. 15 and 16 show that in the large majority of cases the power output exceeds the minimum requirement of 200 W. The worst-case minimum power is 5% low at 190 W. The best-case condition is 35% high at 256 W. The average noon power outputs of the limiting conditions shown are 17% high at 223 W. At the higher solar intensities that occur during the spring and fall seasons, the power level is above 200 W for all conditions.

The power-to-weight ratio varies with the power output of the array at noon at a specific Martian location. The range of power outputs for the first day of summer (lowest solar intensity) are shown for the noon conditions in Figs. 15 and 16. The array weight breakdown is:

Mechanical (solar panel, adhesives, supports, frames, deployment mechanism, etc.).	33.07 lb
Electrical (solar panel and adhesives).	23.37 lb
Total system weight	56.44 lb

The specific power output is based on the equivalent power at 1 AU. Taking the power output at the worst-case condition of 46 mW/cm² (summer), the following limits are obtained:

$$\text{Summer (maximum)} = 256 \text{ W}$$

$$\text{Summer (minimum)} = 190 \text{ W}$$

Converting to 1 AU by the ratio of 46/140 = 0.328,

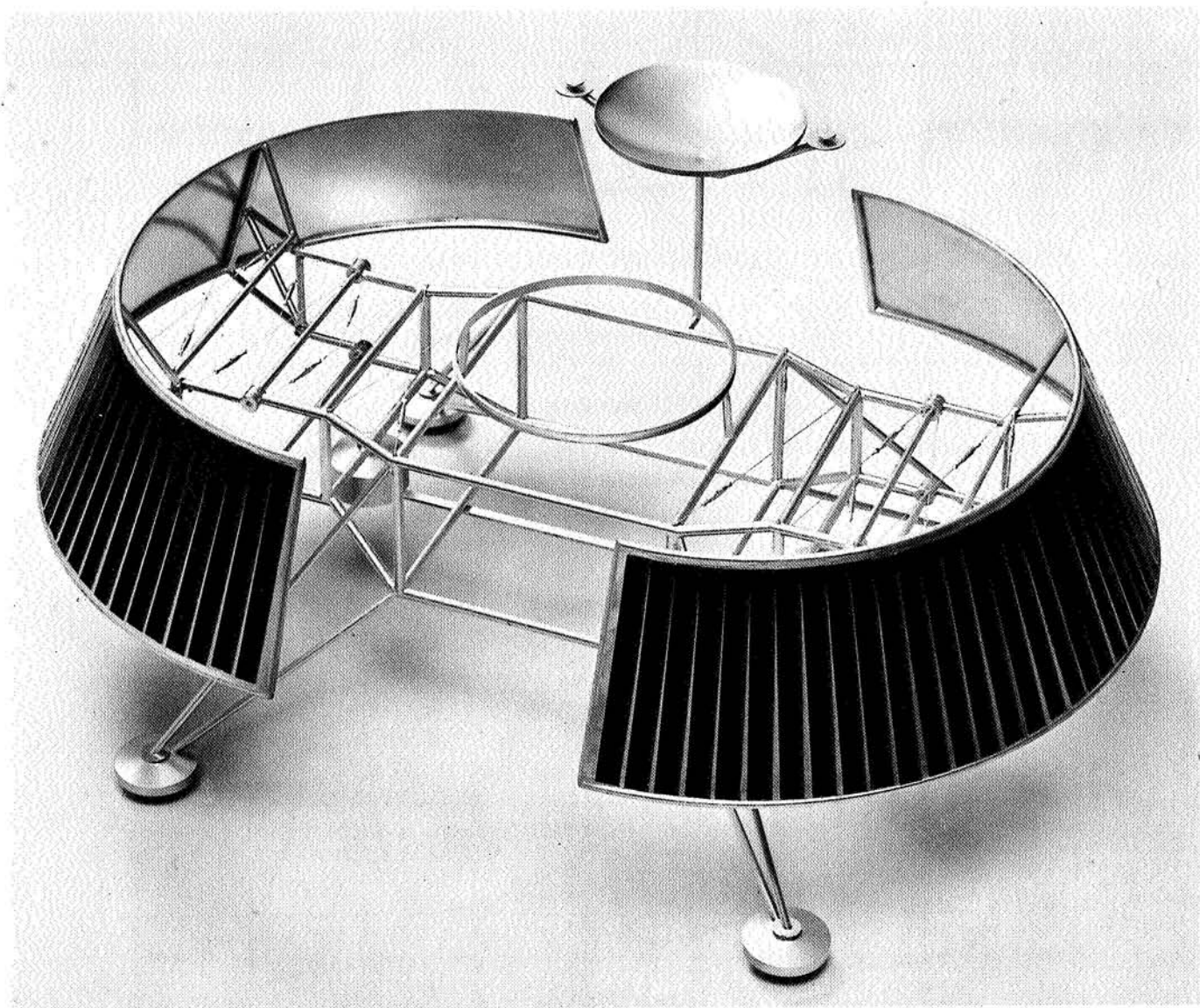$$256/0.328 = 780 \text{ W (1 AU)}$$

$$190/0.328 = 580 \text{ W (1 AU)}$$

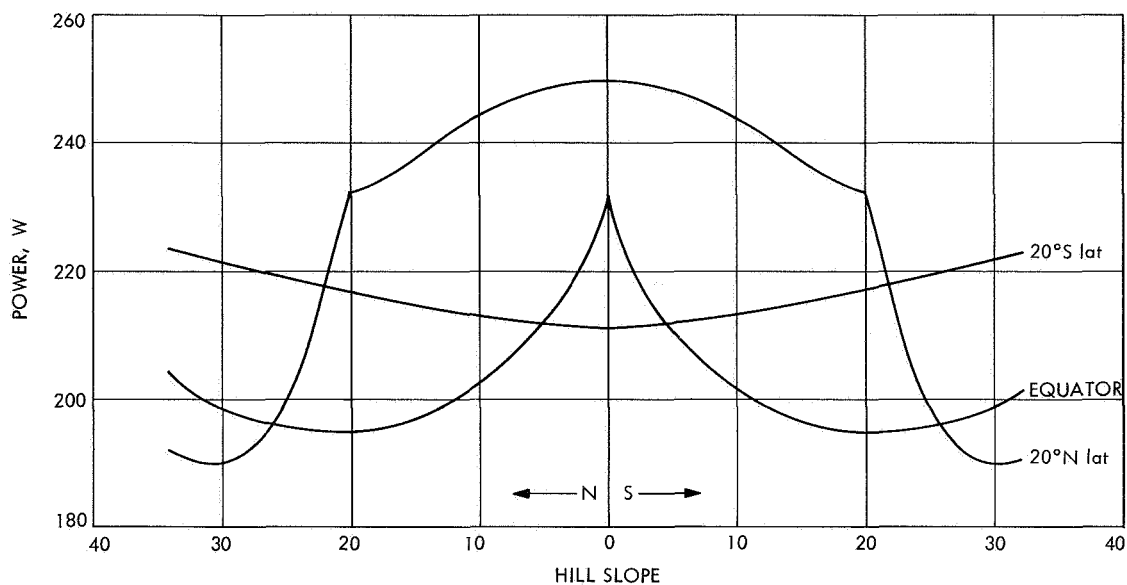Fig. 14. Planetary solar array (non-tracking deployable system)

Fig. 15. Power output at noon for 20°N lat, equator, and 20°S lat vs north–south hill slope for the first day of summer
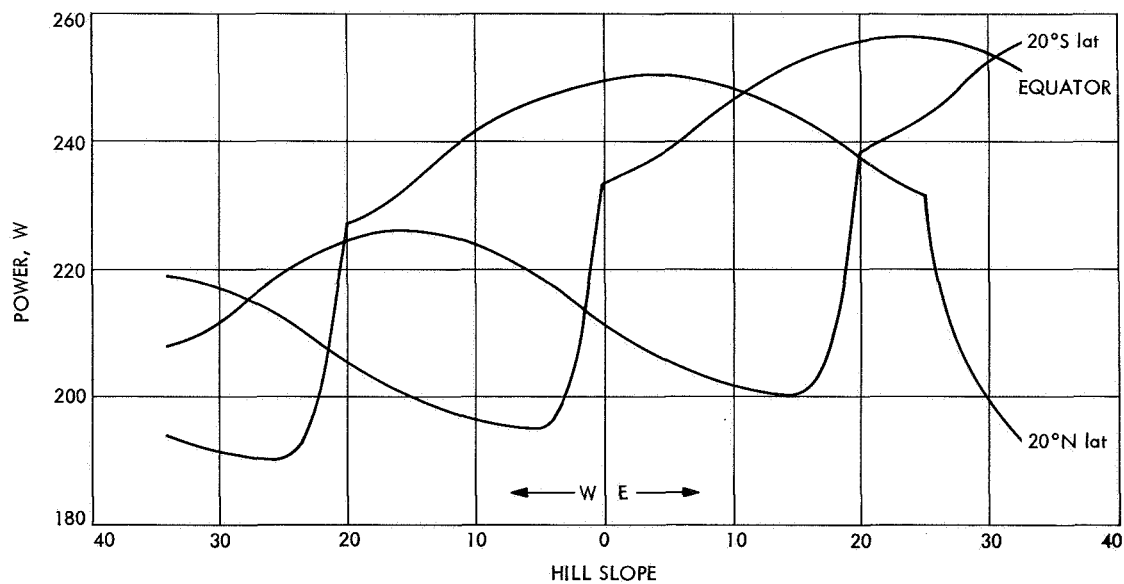

Fig. 16. Power output at noon for 20°N lat, equator, and 20°S lat vs east–west hill slope for the first day of summer

Therefore, the specific power would lie between the range of

$$780/56.44 = 13.8 \text{ W/lb}$$

$$580/56.44 = 10.3 \text{ W/lb}$$

G. Electrolytic Determination of the Effective Surface Area of the Silver Electrode, Part II,
G. L. Juvinall

1. Introduction

A major objective of the continuing study of the reaction geometry of alkaline battery electrodes is the development of new and better methods of measurement of the effective electrolytic surface area of a working electrode. This study is being performed at Brigham Young University under JPL contract; Dr. Eliot Butler is the principal investigator. Earlier results of the surface area studies were reported in SPS 37-39, Vol. IV, pp. 19–21. A new coulometric potentiostatic method is reported here.

2. Measurement Method

The new method of electrode area determination is based upon the charge-acceptance per unit area of smooth standard electrodes. The charge-acceptance can be directly related to the thickness of the oxide layer formed during the oxidation of the silver electrode in alkaline solution. At present, the relationship between the charge-acceptance per unit area and the applied potential in a constant potential oxidation is under study.

Earlier work on the aluminum–aluminum oxide electrode has shown that the charge-acceptance per unit area is the same at identical applied potentials for electrodes of different surface roughness (Ref. 1). Thus, the following equation may be used to calculate surface area:

$$a_{\text{unknown}} = a_{\text{standard}} \frac{q_{\text{unknown}}}{q_{\text{standard}}} \qquad (1)$$

where a = surface area in cm^2 and q = total charge in coulombs. Two oxidation runs are required; then, if the area of one electrode is known, the area of the other can be calculated. The total charge is obtained from the integral of the voltage–time curve. A diagram of the potentiostat and integrator circuit is shown in Fig. 17. Figure 18 is a diagram of the oxidation cell, showing the location of the electrodes. This electrode arrangement minimizes the I–R drop between the reference and working electrodes. The cell was thermostatted at
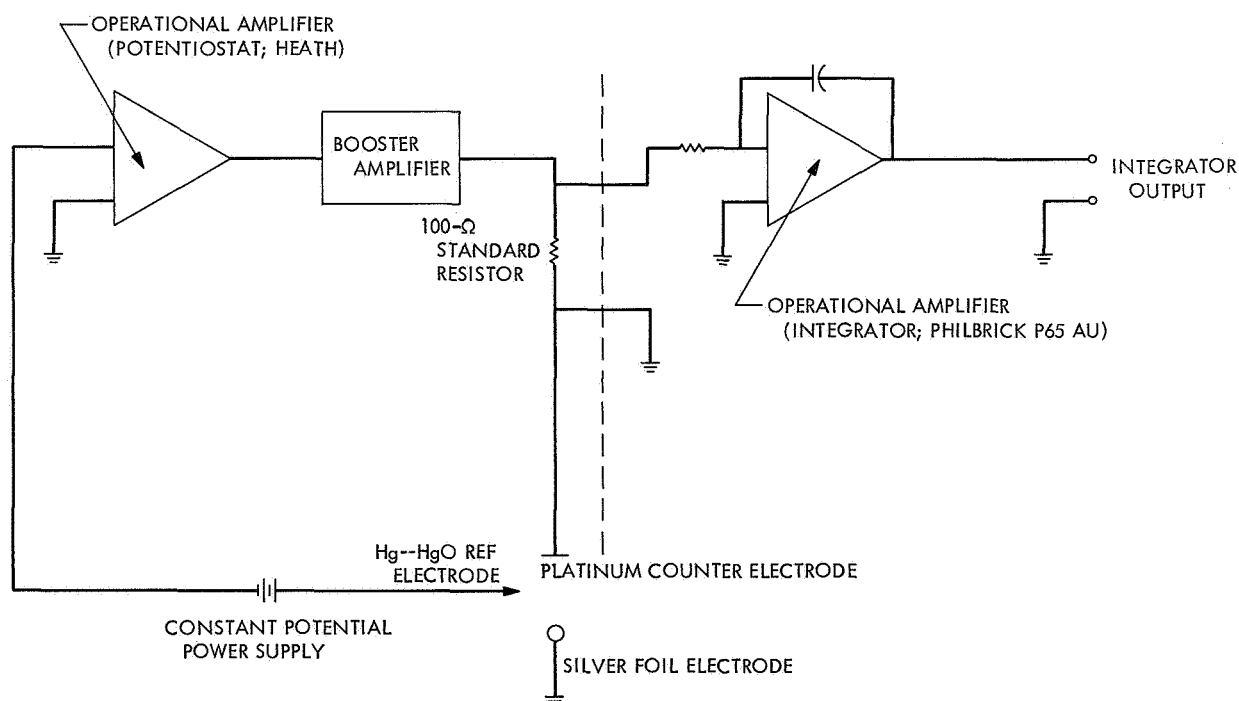

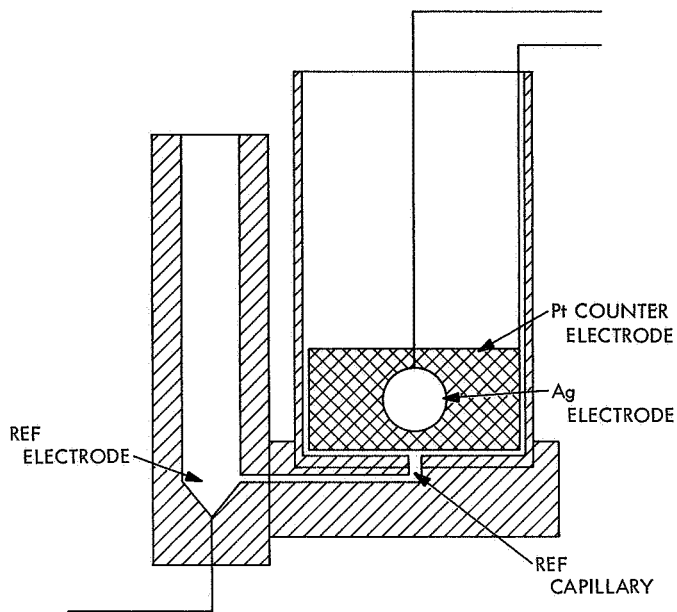Fig. 17. Potentiostat and integrator circuit

Fig. 18. Cross-sectional view of oxidation cell, showing location of working electrodes

Fig. 19. Plot of charge-acceptance per unit area of smooth electrodes vs applied potential

20.0 ± 0.1°C during all oxidation runs. Standard electrodes were prepared by the vapor deposition of metallic silver on smooth glass discs.

3. Results and Conclusions

A plot of charge-acceptance per unit area of smooth standard electrodes versus applied potential is shown in Fig. 19. The purpose of this curve is to indicate acceptable ranges of potential for use in the constant potential estimation of surface area. For example, the region from 0.275 to 0.315 V versus the Hg–HgO reference is not acceptable; there are large changes in charge-acceptance coupled with small changes in applied potential. Conversely, the region from 0.325 to 0.400 V is desirable because of its flatness. Here, small errors in potentiostatic control cause only small variations in charge-acceptance.

Comparison runs were made on silver foil discs of two different geometric areas. Four runs on electrodes of each size were made utilizing the previously reported constant current method (SPS 37-39, Vol. IV), giving a reproducibility in surface area of ±3%. Four runs were also made potentiostatically on electrodes of each size at an applied potential of 0.400 V versus Hg–HgO. The reproducibility in total charge passed was ±7%. These results are in agreement within experimental accuracy.

The effective electrolytic surface areas of the small discs were then calculated, using Eq. (1). The electrolytic area of the large disc as determined by the constant

Table 4. Comparison of foil electrodes in constant current and potentiostatic surface area estimations

Parameter	Foil electrodes cleaned by electropolishing	
	2.53 cm²	0.688 cm²
Effective electrolytic surface area at constant current	2.84 cm² ±3%	0.775 cm² ±3%
Total charge passed in oxidation at 0.400 V vs Hg–HgO	100 mC ±7%	27 mC ±7%
Effective electrolytic surface area at constant potential	2.84 cm²†	0.770 cm² ±7% ‡

†Assumed to be the same as the constant current value. That is, this electrode was used as the standard in this comparison.
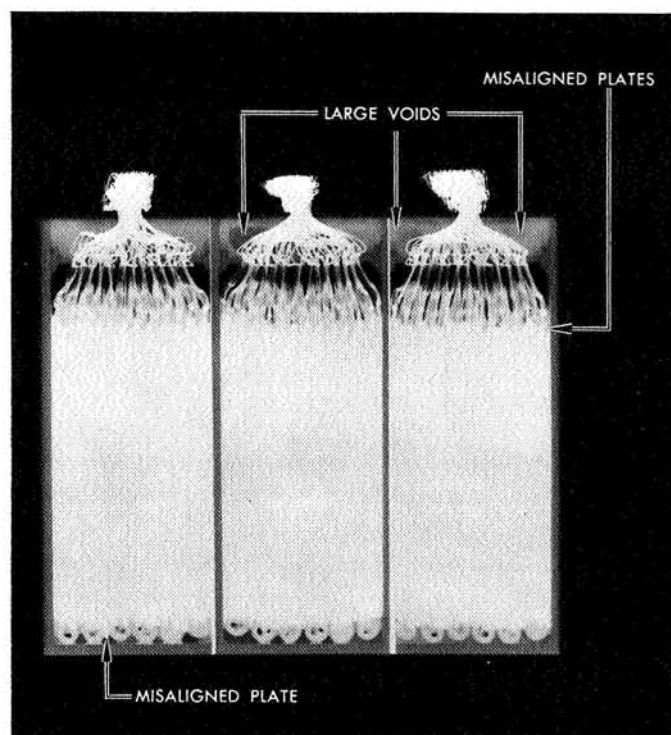
‡Value calculated by using Eq. (1).

current method was taken as the area of the standard electrode for use in the calculation. The results of the calculations are given in Table 4. The method apparently is a very promising one for the electrolytic determination of the effective electrode surface area.

Reference

1. Plumb, R. C., *J. Electrochem. Soc.*, Vol. 105, p. 502, 1958.

H. X-ray Radiography of *Mariner*-Type Battery Cells, S. Krause

1. Introduction

A series of x-ray radiographic studies of *Mariner*-type battery cells has recently been completed at the U.S. Naval Ordnance Laboratory. These studies represent part of a continuing effort to improve the manufacturing processes used in fabricating flight batteries.

It is important to improve the uniformity of the cells in order to achieve higher in-flight reliability as well as more accurate interpretation of laboratory test data. The use of x-ray radiography as a quality-control tool can help to achieve this goal.

Fig. 20. X-ray side-view of a three-cell monoblock, showing large voids and misaligned plates

The two preliminary problem areas that were examined in the course of this effort were cell seals and plate alignment. Both can affect cell performance.

A 250 kV General Electric x-ray camera has been used to x-ray over 50 monoblocks (150 cells).

2. Cell Seals

Plate lead wires are positioned through a subcover and an upper cover. Between these two covers is a cavity which is filled with an opaque potting material to seal around the 25 lead wire bundles. Voids and defects in the areas around the wires allow cell leakage to occur more rapidly during environmental or cycling tests, and thus affect the test results adversely.

An example of the x-ray side-view of a three-cell monoblock may be seen in Fig. 20. This x-ray shows what appear to be voids in the upper cavity around the plate lead wires. In a sealed silver–zinc cell (the *Mariner* cell is this type) it is necessary to prevent electrolyte leakage

resulting from the electrolyte "wicking up" the plate lead wires to the external environment. This condition results in degraded performance and ultimate failure. Encapsulation around the plate lead wires prevents such electrolyte leakage. Voids in the potting material around the plate lead wires substantially reduce the impeded leakage path to the outside of the cell. Variations in the size, number, and location of these voids could cause cell failures due to leakage that would occur at different rates and under different conditions. Defects of this nature could influence the evaluation of a design for a flight battery.

A monoblock was progressively dissected in a serial cross-section manner, parallel to the plane of the x-ray view seen in Fig. 20. The results of this sectioning showed the presence of large voids, as seen in one section in Fig. 21. The size, shape, and location of the voids were accurately predicted by the x-ray radiographs.

When the existence of voids of this nature was confirmed, a number of changes in the potting process were
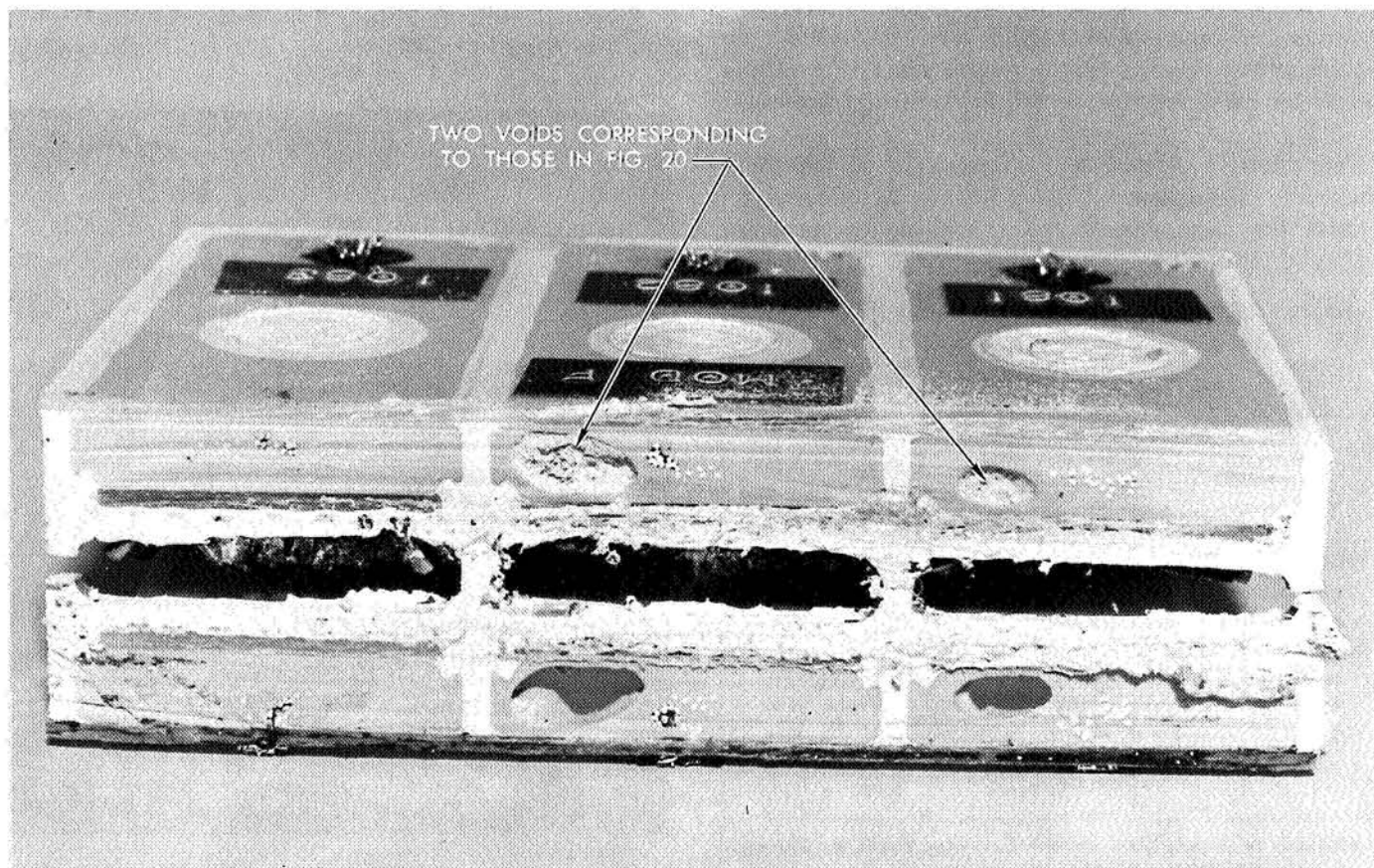

Fig. 21. Results of sectioning three-cell monoblock, showing large voids

instituted. Subsequent production and x-ray analysis of more cells resulted in the type of upper cavity potting shown in Fig. 22. The process changes virtually eliminated all voids, so that in all the newly fabricated cells, the seals in this area are as alike as possible.

3. Plate Alignment

Although the cell case is visually inspected after plate insertion, considerable plate-pack misalignment can result because of process variations and inspection limitations. Subsequent cycle data can be affected by misaligned plates.

The misalignment of cell plate packs can affect cell capacity if portions of the active electrode surface areas are not fully reacted. Figure 20 shows the three-cell monoblock with plates misaligned in the vertical direction. Note the large variation between the tops of some adjacent plates. It is quite possible that these cells would not perform as well as others with better plate alignment, particularly after several cycles. This condition would then cause considerable spread in capacity data and hinder the completion of an accurate design evaluation.
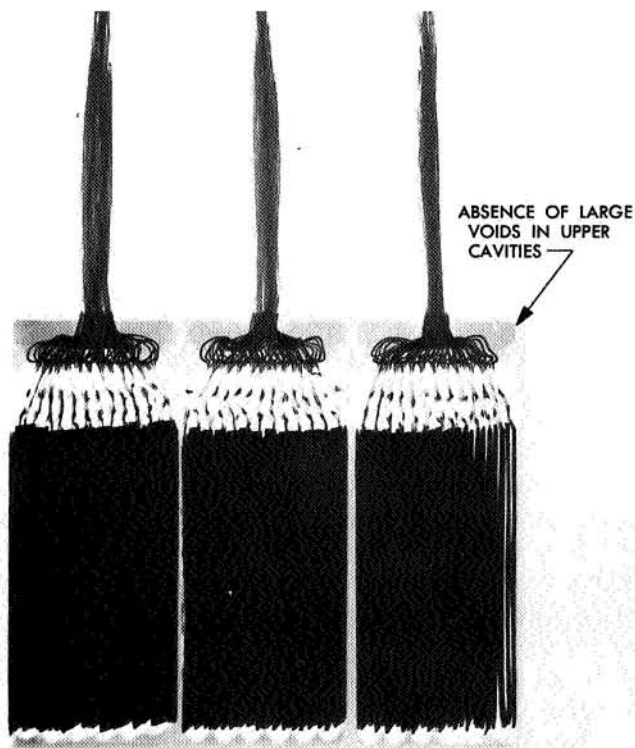

ABSENCE OF LARGE VOIDS IN UPPER CAVITIES

Fig. 22. X-ray side-view of a three-cell monoblock, showing absence of large voids after changes in potting process

4. Conclusions

Although at present in-process x-ray of plate alignment is not possible, future production procedures might be modified to include this type of inspection and allow a realignment step. Certainly, such a procedure would make the cells as alike as possible, allowing better comparison of test results. If the realignment step proves to be impractical, then at least the x-ray catalogue of every cell used in a test program would aid in pointing out those differences in performance or failure rates that were due to structural inconsistencies rather than to actual design deficiencies.

I. Calorimetric Measurements on the *Surveyor* Main Battery, W. L. Long

1. Introduction

The mission requirements of future JPL space programs may be expected to impose increasingly severe operating constraints on the spacecraft power system. A battery system designed for a long, sophisticated mission, such as a multiplanet probe, will necessarily be operating much closer to the performance limits than ever before. In addition, more complicated environmental and component compatibility problems arise.

Calorimetric data on spacecraft components are always required for proper thermal control. Heat generation by most electrical components is obtained from input–output efficiencies, and, for a constant power level, the heat generated is fairly constant. However, the heat generated by a silver–zinc battery varies with state of charge as well as with power level, and accurate calorimetric data will be necessary for future spacecraft design studies. Preliminary work in this area has been previously reported (Ref. 1). This work is being continued by Hughes Aircraft Co. under JPL contract.

2. Battery Description

The *Surveyor* main battery, as manufactured by ESB Co., is a 150 A-h, 14-cell, sealed silver–zinc battery. The cell cases are constructed of polystyrene; the battery case is magnesium. The total weight of the flight battery is 46.5 lb.

3. Measurement Technique

Calorimetric measurements have thus far been performed at discharge rates of 5 and 18 A. All measurements to date have been performed at 118°F. The calorimeter is isothermal, operating at a boiling point

of a liquid which surrounds the battery and fills the calorimeter. The liquid is heated by automatic pre-calibrated electric heaters, and thus maintained at the boiling point automatically. When heat is given off or absorbed by the battery, the change in power furnished to the heater is automatically recorded. When steady-state operation is reached, the change in power is the heat generated (or absorbed) by the battery. Provisions are included for maintaining constant pressure, constant rate of vaporization, and for the return of condensed vapor at a constant temperature. Freon F-113 was used for these tests.

4. Results

The results of the preliminary measurements show that the *Surveyor* battery produces heat equivalent to 5 W of power during a 5-A discharge. The battery produces heat equivalent to 80 W of power during an 18-A discharge. These results are based on steady-state operation. It is apparent that the heat evolution increases very sharply with an increase in discharge rate.

Further studies will extend the measurements to different discharge rates and temperatures, as well as define the effects of state of charge on heat generation by the battery.

Reference

1. Rowlette, J. J., "Heat Generation in the *Surveyor* Main Battery", Paper No. 47, The Electrochemical Society Fall Meeting, Oct. 1967.

J. Six-Converter Solar Thermionic Generator,
O. S. Merrill

1. Introduction

This is a summary of the work performed by Thermo Electron Corp., Waltham, Mass., under JPL contract during the period from Jan. 10, 1967 through Mar. 31, 1968 (Ref. 1). The work reported includes the design and fabrication of a six-converter solar thermionic generator designated as JG-4, and the design, fabrication, and performance testing of twelve identical converters, six of which were incorporated into the generator. The generator is to operate in a solar-energy concentrating system consisting of a parabolic mirror of 57-in. rim radius and a 69-in. focal length. The mirror generates a solar image in the form of a circular ellipsoid which at the focal plane of the mirror has a cross-sectional area of about 0.885 in.^{2} and an approximate maximum energy

of 5000 W at 1 AU. The design of the six converters is similar to that of the series VIII converters (used in previous solar generators; SPS 37-40, Vol. IV, pp. 1–14) but has been modified to be compatible with a six-converter system. The converters have planar electrodes with a Re emitter and Mo collector. The emitter area is 2 cm^2. The converters are designed to operate at an emitter temperature of 2000°K at an interelectrode spacing of 2 mils.

2. Generator

A detailed review and evaluation was made of the original generator design.[1] This was necessitated by tests conducted at JPL subsequent to the original design which showed that solid Re emitters and Re sleeves were more reliable for extended operation than the Ta substrate pressure-bonded Re emitters and Ta sleeves proposed in the original design. However, incorporating solid Re emitters into the converters of the generator required redesign of the generator cavity because of the lower thermal conductivity of Re. The new design has the rear surfaces of the six emitters (Re) forming a cylindrical cavity of 0.61-in. radius and 0.658-in. length. The front opening of the cavity is to be placed at a distance of about 0.4 in. behind the mirror's focal plane, i.e., towards the sun. This produces optimum impingement and absorption of the solar energy on the cavity wall.

A tungsten cone with a 1-in. diameter opening protects the cavity walls from adverse effects caused by misalignment of the generator and the mirror. The rear of the cavity is formed by a highly reflective electropolished W surface in the form of an inverted, doubly truncated cone (back-piece), so designed as to direct reflected solar energy uniformly to the cavity wall (the emitters). This back-piece reflector is thermally isolated from the converters. The energy absorbed by the reflector is dissipated by a large Cr$_2$O$_3$-coated Mo radiator which is brazed to the W piece by a high-temperature braze. During solar operation, the W back-piece is designed to operate at a temperature less than 1200°C. With this solar image–cavity arrangement, which is expected to result in a near-optimum generator performance, approximately 4500 W of solar energy enter the cavity; 200 W are absorbed by the front piece; 2300 W are absorbed by the six Re emitters; 1400 W are absorbed by the W back-piece; the remaining 600 W are reflected and/or re-radiated and escape through the front opening of the cavity.

---

[1]JG-4, discussed in Thermo Electron Corp. Report TE 18-66, JPL Contract 951230.

Considerable effort was devoted to the generator assembly, which required the fabrication of special tools for aligning to critical tolerances the converters and the back-piece which form the cavity. Prior to constructing the Mo block, to which the various parts of the generator were mounted, an Al model was fabricated and checked for feasibility of the overall block design.

Other work performed in association with the JG-4 included the evaluation of the thermal transfer characteristics of the 0.65 Pd–0.35 Co braze selected for joining the W and Mo parts of the cavity back-piece. For this purpose, two samples, identical in geometry, were prepared and tested. One sample consisted of a W and a Mo disk joined together with the 0.65 Pd–0.35 Co braze; the other sample was a solid Mo disk. Both samples were tested under identical conditions, and comparison of the test results indicated that the rate of heat transfer in the W–braze–Mo sample was equal to or slightly higher than that measured in the all-Mo sample.
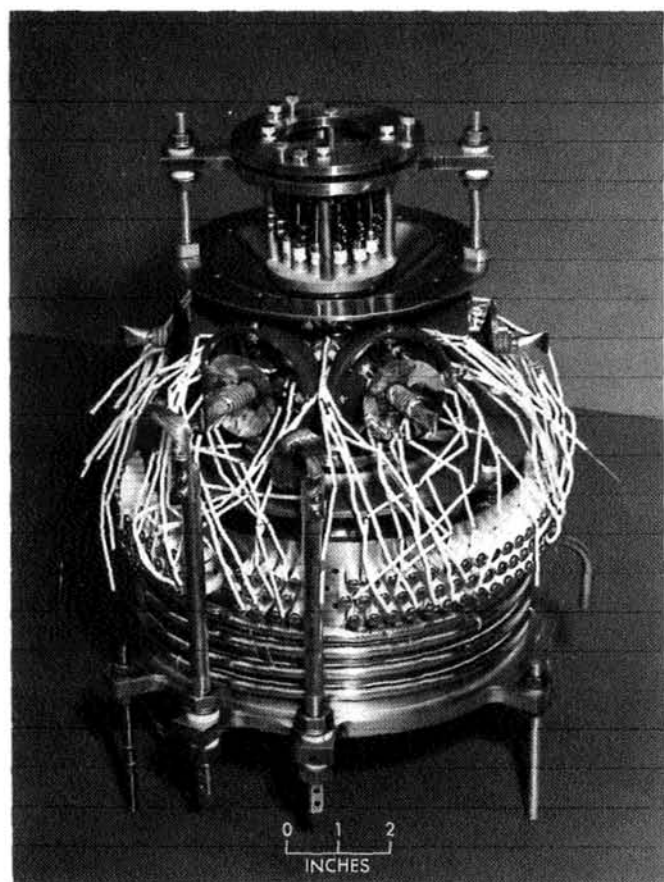
The completed generator (JG-4), with the electron bombardment unit attached for electrically heating the generator during laboratory testing, is shown in Fig. 23. Figure 24 shows a close-up of the generator cavity.

3. Converters

Twelve identical thermionic converters (Fig. 25) were fabricated and individually tested; six of these converters were incorporated into the generator. During the test of each converter, the output current was measured at different output voltages and at given emitter temperatures, with the cesium temperature optimized for maximum output. All twelve converters generated nearly identical data. The current–voltage data indicate an average power output of 37.5 W from each converter, or a total of 225 W from the six converters used. The same power output was obtained at a lower emitter temperature but also at a lower output voltage. The performance characteristics of the six converters used in the generator are shown in Fig. 26.

Considerable effort was expended in the preparation of the Re sleeves, which developed vacuum leaks during
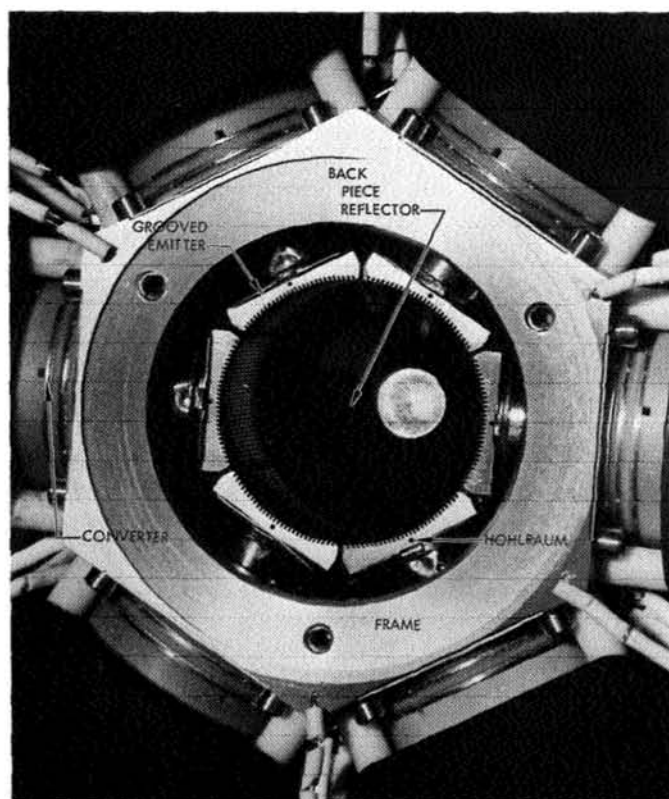

Fig. 23. Complete JG-4 generator with
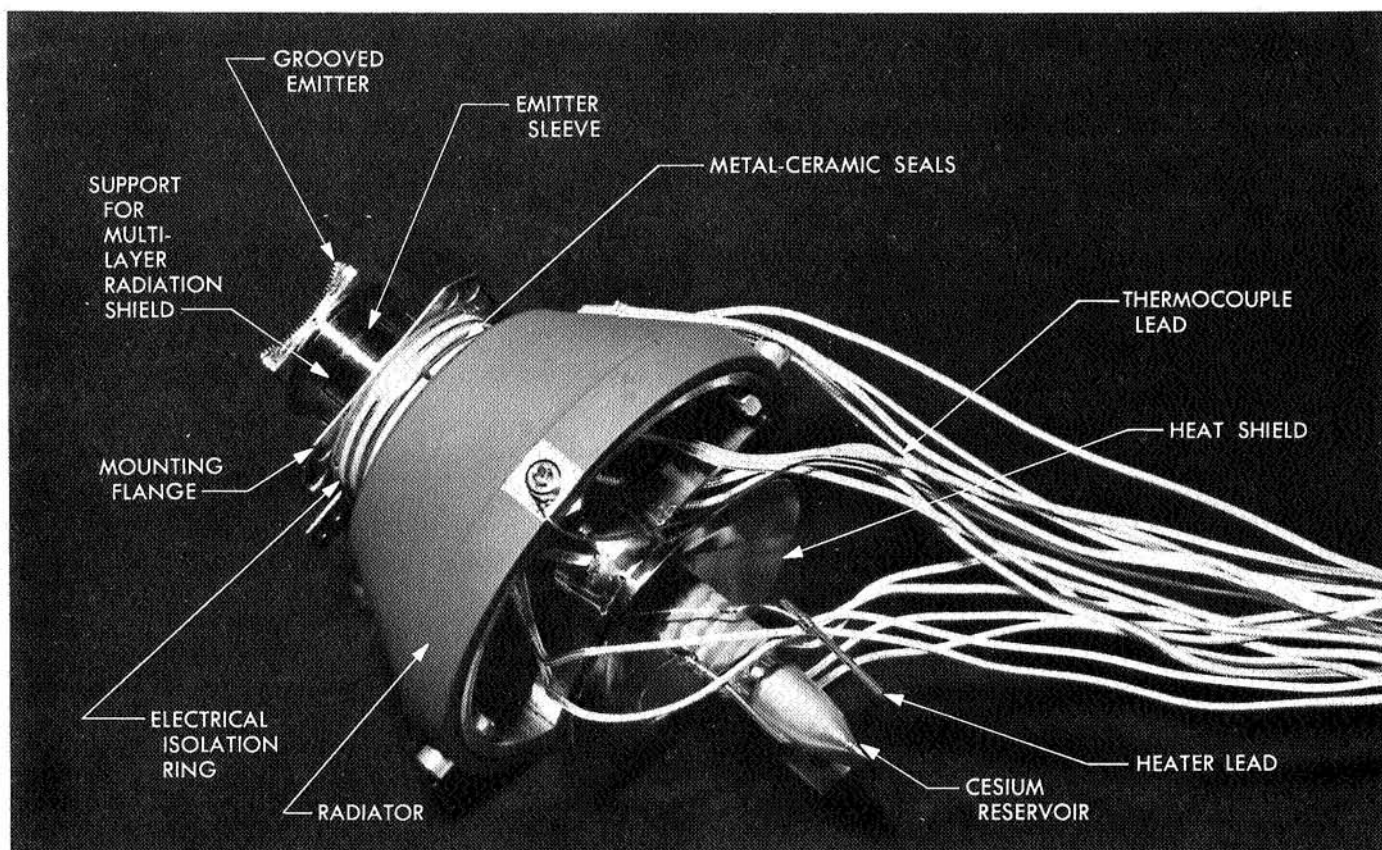electron-bombardment unit

Fig. 24. JG-4 generator cavity

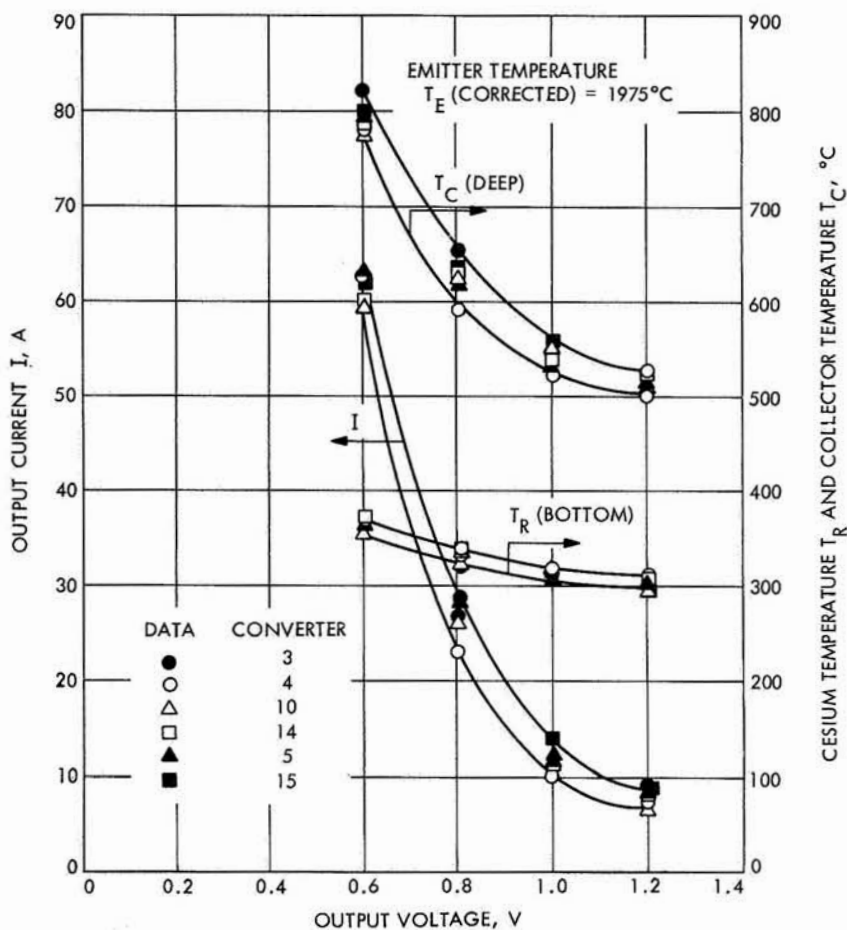**Fig. 25. Thermionic converter used in JG-4 generator**

Fig. 26. Performance characteristics of six converters used in JG-4 generator

machining or thermal cycling. These leaks resulted from voids left in the seam of the Re tubing during the heliarc-welding process conducted by the vendor. This problem was eliminated after the Re tubing was purchased from the vendor in the "rolled only" state and the seam was electron-beam-welded by TECO. Substantial effort was also expended in the fabrication of the emitters which, due to their complex geometry and extremely close tolerances, required special preparatory techniques, particularly during electron discharge machining and subsequent processing.

4. Electron Bombardment Unit

For laboratory tests of the JG-4, an electron bombardment unit (Fig. 27) was fabricated and tested. This unit consists of six hairpin tungsten filaments arranged to form a cylindrical unit suitable for insertion into and heating of the generator cavity. The W filaments can be connected either in parallel, and controlled as a single unit, or individually, and controlled as six separate units. The unit was tested inside a cylindrical Mo block having approximately the same geometry as the generator cavity.
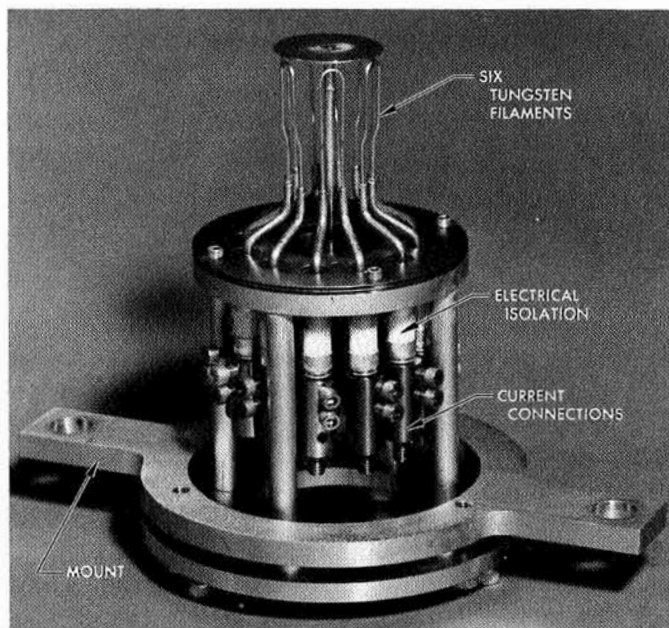

Fig. 27. Electron-bombardment gun used for laboratory test of JG-4 generator

The test results indicated that for a temperature of about 2000°K on the Mo surface facing the filaments, a total output power of 2200 W was required from the filament assembly.

Reference

1. Athanis, T., Shefsiek, P., and Lazaridis, L., *Final Report, Six-Converter Solar Thermionic Generator*, Report TE4073-146-68. JPL Contract 951770, Thermo Electron Corp., Waltham, Mass., June 1968.

K. Power Conversion Circuit Development,
D. J. Hopper

1. Introduction

The objective of the power conversion circuit development task is to develop advanced technology power conditioning components, i.e., regulators, inverters, battery chargers, etc., capable of meeting JPL advanced mission requirements.

The most recent activity on this task has been to develop a boost regulator with characteristics that are significantly better than the characteristics presently available in the *Mariner* spacecraft boost regulators. In particular, efficiency, transient response, and a reduced number of component parts were all goals of this regulator development program.

The work described below was performed under JPL contract by Wilorco, Inc., Long Beach, Calif.

2. Regulator Requirements and Description

The design requirement goals for the boost regulator are shown in Table 5. Three power levels were of interest: 100, 200, and 400 W. Figure 28 shows the functional block diagram for the regulator design that was developed.

When Q1 is turned on, the current in the left side of T1 will increase, and, due to transformer action, the voltage on the right side of T1 will also increase. When the voltage reaches a set level (56 V), the error amplifier signals the drive amplifier. The drive amplifier then turns Q1 off. The voltage out of T1 will then start to decrease. When the voltage decreases sufficiently, the error amplifier signals the drive amplifier to again turn Q1 on. The cycle then repeats. The input and output filters are inductance-capacitance type filters.

The error amplifier is a differential amplifier using a zener diode reference. As can be seen in Fig. 28, the

Table 5. Boost regulator design requirements

| Parameter	Specification characteristic
Input	
Input voltage, V	25 to 50
Reverse polarity protection	Yes
Environmental	
Operating temperature range, °C	−10 to 75
Survival temperature range, °C	−55 to 145
Degraded performance range, °C	−40 to 100
Output	
Efficiency (min), %	90
Regulation (line, load, and temperature variation), %	±½
Output voltage, Vdc	56
Output ripple, mV rms	less than 50
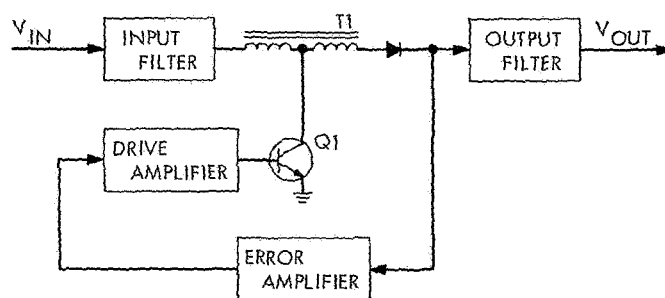
Fig. 28. Boost regulator block diagram

Q1, T1 combination only has to supply voltage in excess of the input voltage, $V_{out} - V_{in}$. This keeps the power switched by Q1 to a minimum. Since Q1 is switching relatively small quantities of power, the efficiency of this type of circuit can be quite high.

The performance characteristics of the 200-W regulator, which are typical of those obtained for the other power levels, are shown in Table 6 along with the characteristics of the *Mariner* Mars 1969 boost regulator. The *Mariner* Mars 1969 boost regulator uses magnetic amplifier control, while the developed boost regulator uses solid-state control. This means that the transient response of the developed boost regulator is better than that of the *Mariner* Mars 1969 boost regulator. There are 66 parts in the new regulator; the *Mariner* regulator has 74 parts.

3. Conclusion

Because of the increase in efficiency, regulation, and transient response and the reduction in parts, the newly

Table 6. Boost regulator performance characteristics

Parameter	Actual characteristics	
	New 200-W regulator	Mariner Mars 1969 regulator
Efficiency, %	93 to 97	87 to 93
Regulation, %	±0.5	±1
Voltage, V	56	56
Output power, W	200	250

developed boost regulator is a significant improvement over the existing *Mariner* design.

L. Electric Propulsion Power Conditioning,
E. Costogue

1. Introduction

The electric propulsion power conditioning effort is directed towards the design and procurement of hardware for two programs—SEPST II and III.[2]

The SEPST II program will utilize one breadboard power conditioner unit. This breadboard was built for the SERT II program[3] and is being modified to present power requirements. Hughes Aircraft Co. has been contracted to modify the unit and the test console which will be used to qualify the power conditioner.

The SEPST III program will utilize one breadboard and two experimental power conditioner units. Hughes Aircraft Co. has been contracted to design, develop, fabricate, and qualify-test the units.

---

[2]SEPST = solar electric propulsion system test.
[3]SERT = space electric rocket test.

2. Power Requirements and Characteristics

The power requirements for the power conditioner unit are shown in Table 7. There are two groups of power supply—Group I, low-voltage supply, and Group II, high-voltage supply.

Figure 29 shows the preliminary power conditioner unit block diagram, identifying the modules necessary to generate the voltages and currents required by the thrusters.

A line regulator is provided to generate 35-V regulated power from the 40- to 80-V line, which in turn drives the 5-kHz heater inverter. The output of the heater inverter is fed to the following modules: neutralizer heater, neutralizer keeper, vaporizer heater, and magnet.

The cathode heater power is supplied by a 5-kHz inverter. A standby inverter is provided to supply the power when a failure is detected. The output of the operating inverter is fed to the cathode filter module for filtering and control.

A master oscillator and phase shift module are utilized to provide base drive to all screen inverters. Phase shift is required to stagger the outputs of the screen supply inverters. The screen power is supplied by eight 12.5-kHz inverters. The output of the inverters is fed to the screen filter module for filtering and control.

The arc power is supplied by a 12.5-kHz inverter. A standby inverter is provided to supply power when a failure is detected. The output of the operating inverter is fed to the arc filter module for filtering and control.

Similarly, the accelerator power is supplied by a 12.5-kHz inverter and a standby inverter. The output of the operating-accelerator inverter is fed to the accelerator filter module for filtering and control.

Table 7. Power conditioner unit requirements

Group	Power supply	Type	Output	Maximum ratings			Nominal ratings					Range of control,[b] A	Frequency, kHz	
				Energy, V	Current, A	Current limit,[a] A	Energy, V	Current, A	Power, W	Regulator, %	Peak ripple, %		Output	Ripple
I	Magnet manifold heater	dc	Fixed	19	0.85	0.9	15	0.67	10.5	1.0 (current)	5	—	—	10
	Cathode heater	ac	Variable	5	40	45	4.5	35	160	Loop	—	10–40	5	—
	Neutralizer heater	ac	Variable	12	3.4	4	12	2.8	35	Loop	—	0.3–3.4	5	—
	Neutralizer keeper	dc	Fixed	300 V at 5 mA	0.02 at 30 V	0.55	10	0.50	5	1.0 (energy)	2 at 30 V 5 at 10 V	0.02–0.5	—	10
II	Vaporizer	ac	Variable	10	2	2.05	5.5	1.1	6	Loop	—	0.5–1.2	5	—
	Arc	dc	Variable	150 V[c] at 20 mA	7 at 36 V	8	34.5	6	210	1.0 (energy)	2	2–7	—	30
	Beam	dc	Variable	2050	1.0	1.05	2000	1.0	2000	1.0 (energy)	5	0.5–1.0	—	30
	Accelerator	dc	Variable	2050	0.1[d]	0.105	2000	0.01	20	1.0 (energy)	5 at 0.1 A	—	—	30

[a]Exact values to be specified by the manufacturer.

[b]Current varies as function of engine loop control:
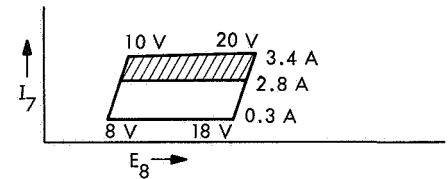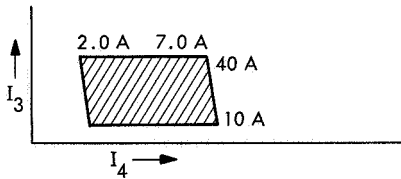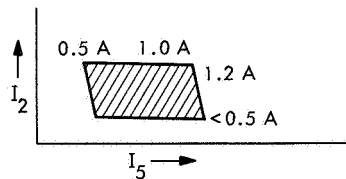
[c]Starting characteristics: 150 V to 36 V at 20 mA.

[d]Current stays at this level for less than 10 min at very low repetition rate.

Fig. 29. Power conditioner unit block diagram